International Geology Review, 2015
Vol. 57, Nos. 9–10, 1189–1217, http://dx.doi.org/10.1080/00206814.2014.905997

Taylor & Francis
Taylor & Francis Group

Multiple Mesozoic magma processes formed the 240–185 Ma composite Weishan pluton, South China: evidence from geochronology, geochemistry, and Sr-Nd isotopes

Xing Ding[a]*, Wei-Dong Sun[b], Wei-Feng Chen[c], Pei-Rong Chen[c], Tao Sun[c], Sai-Jun Sun[b,d], Chiou-Ting Lin[a,d] and Fu-Kun Chen[e]

[a]*State Key Laboratory of Isotope Geochemistry, Guangzhou Institute of Geochemistry, Chinese Academy of Sciences, Guangzhou, PR China;* [b]*CAS Key Laboratory of Mineralogy and Metallogeny, Guangzhou Institute of Geochemistry, Chinese Academy of Sciences, Guangzhou, PR China;* [c]*School of Earth Sciences and Engineering, Nanjing University, Nanjing, PR China;* [d]*University of the Chinese Academy of Sciences, Beijing, PR China;* [e]*CAS Key Laboratory of Crust-Mantle Materials and Environments, School of Earth and Space Sciences, University of Science and Technology of China, Hefei, PR China*

(*Received 13 December 2013; accepted 15 March 2014*)

Mesozoic granitic intrusions are abundant in the South China Block (SCB). Understanding the generation of these granitic intrusions is important to better constrain tectonic regimes and mineralization processes. We studied the Weishan pluton, one of the largest Mesozoic composite granitic complexes in Hunan Province, to probe the relationship between multiple magma processes and tectonic events induced by plate interactions. The samples can be classified into three groups. Group 1 is highly fractionated and weakly peralumious, with flatter REE patterns and more negative Eu, Ba, Sr, P, and Ti anomalies compared with other groups. Group 2 is peralumnious-metaluminous while Group 3 is peraluminous, but with higher MgO, FeO, $\varepsilon_{Nd}(t)$, and lower initial $^{87}Sr/^{86}Sr$ in Group 2 than in Group 3. Whole-rock and biotite compositions from all groups define a good linear trend, with Group 1 and Group 2 samples defining two mixing end-members. Single-grain mica Rb-Sr isochron and LA-ICP-MS zircon U-Pb ages show that Group 1 formed at ca. 240–230 Ma, Group 2 at 220–215 Ma, and Group 3 during two episodes at 210–205 Ma and 185 Ma. Integrated geochemical studies suggest that precursor magmas of the three groups were emplaced under oxidizing conditions at relatively low temperatures (<830°C). These magmas were mainly derived by partial melting of Palaeoproterozoic psammites but subsequently differentiated by fractional crystallization, crustal contamination, and remelting. Considering regional tectonothermal events, it is proposed that the oldest Group 1 granitic melts were derived by low-degree partial melting of thickened Palaeoproterozoic psammitic materials during prograde metamorphism due to the collision of the Indochina Block (ICB) and the SCB. The slightly younger Group 2 granitic melts were generated by further partial melting in response to stress relaxation in the post-collision stage and conductive heating from underplating mafic magma. The youngest Group 3 melts represent remobilized buoyant magma pulses supplied from a mushy Group 2 magma source accompanying regional reheating, possibly associated with the uplift of the SCB following its deep subduction during the Dabie orogeny and the subduction of the Palaeo-Pacific oceanic plate beneath the Eurasia plate, respectively.

Keywords: composite granite; Indosinian; Yanshanian; South China; Mesozoic

1. Introduction

It is generally assumed that the South China Block (SCB) experienced successively two important tectonic events in the Mesozoic, including (1) an early Mesozoic compressional and metamorphic event related to the Indochina Block (ICB)-SCB collision (Indosinian orogeny) (Wong 1929; Lepvrier *et al*. 1997; Carter *et al*. 2001; Wang *et al*. 2007) and (2) a late Mesozoic extensional and regional compressional deformation event related to the westward subduction of the Palaeo-Pacific plate (Yanshanian orogeny) (Wong 1929; Ren and Chen 1989; Zhou *et al*. 2006; Li and Li 2007). As a major register of the Indosinian orogeny on the SCB, early Mesozoic granitoids, which are known as Indosinian granitoids, are exposed mainly as dispersed plutons in Hunan, Jiangxi, and Guangxi Provinces (Figure 1), with a total outcrop area of around 14,300 km^2 (Zhou *et al*. 2006). The granitoids were later often intruded by late Mesozoic (Yanshanian) granites with strongly peraluminous composition and fine-grained texture, thus forming a series of composite intrusive complexes (HNGBMR 1988; Zhou *et al*. 2006). The petrogenesis of these composite complexes and their tectonic settings remain poorly constrained (Hsü *et al*. 1990; Gilder *et al*. 1996; Guo *et al*. 1997; Wang *et al*. 2005a; Ding *et al*. 2006; Li *et al*. 2006; Wang *et al*. 2006; Zhou *et al*. 2006; Li and Li 2007; Dai *et al*. 2008; Metcalfe 2009; Chen *et al*. 2011), and even whether they were derived from different sources or not is still highly debated (Chen *et al*. 2006; Chen *et al*. 2007a, 2007b; Wang *et al*. 2007; Ding *et al*. 2012).

Mesozoic granitic complexes, in particular, the Indosinian granites, are widely distributed in Hunan

*Corresponding author. Email: xding@gig.ac.cn

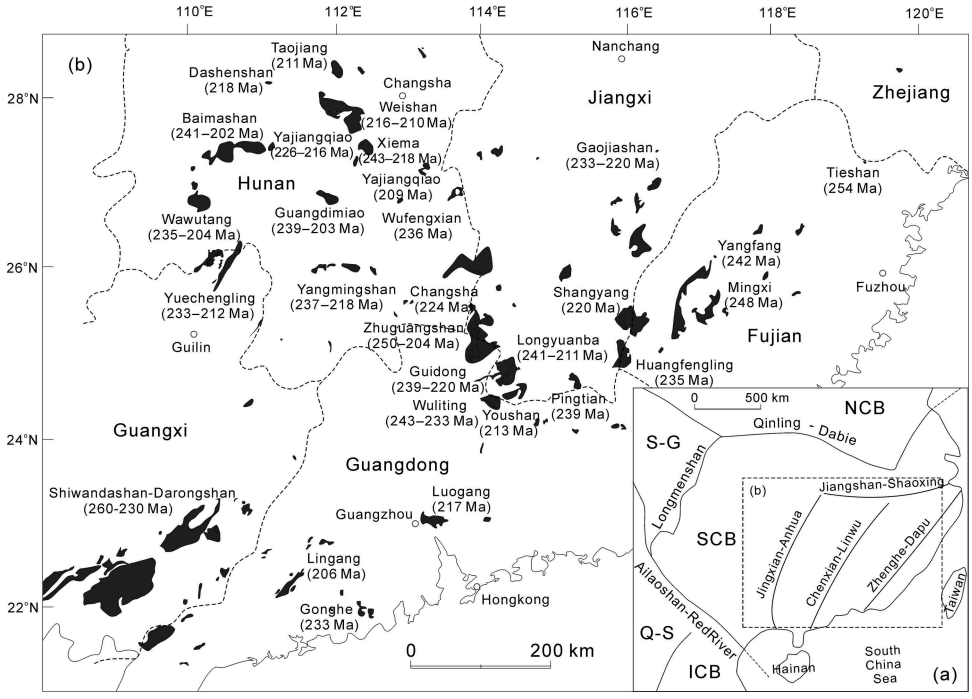

Figure 1. Major distributions of Indosinian granitoids in South China. (a) Distributions of principal continental blocks of present-day Southeast Asia and boundaries on the blocks, modified after Li *et al*. (2006). Abbr. as follows: SCB, South China Block; NCB, North China Block; ICB, Indochina Block; S-G, Songpan-Garze Fold Belt; Q-S, Qiangtang-Sibumasu Block. (b) Distributions of Zircon U-Pb ages and plutons for Indosinian granitoids, modified after Zhou *et al*. (2006). U-Pb age data are from (Xu *et al*. 2003; Deng *et al*. 2004; Qiu *et al*. 2004; Zhang *et al*. 2004; Sun *et al*. 2005; Wang *et al*. 2005a; Chen *et al*. 2006, 2007a, 2007b; Ding *et al*. 2006; Wang *et al*. 2007; Sun *et al*. 2010; Cao *et al*. 2011; Han *et al*. 2011).

Province with an outcrop area of around 8000 km^2 (HNGBMR 1988). In this article, we present new single-grain mica Rb-Sr isochron ages, LA-ICP-MS zircon U-Pb ages, and mineralogical, geochemical, and Sr-Nd isotopic data for Indosinian-Yanshanian granites of the Weishan pluton, one of the largest Mesozoic composite granitic complexes in Hunan Province. These results add important constraints to the relationship of tectonic and magmatic evolution among the multistage granitoids, as well as the Mesozoic tectonic evolution of the SCB.

2. Geological background and petrography

Mesozoic intrusive and volcanic rocks in the southeastern SCB are found mostly in Zhejiang, Fujian, Guangdong, Jiangxi, and Hunan Provinces, with a total outcrop area of around 218,000 km^2 (Zhou *et al*. 2006). Therein, Indosinian rocks are mainly exposed in the SCB interior with systematically increasing ages outward from the Late Triassic to the Middle Triassic, and finally to the Early Triassic (Figure 1(b)). Yanshanian rocks are distributed closer to the coast, with systematically decreasing ages outward from the Early Jurassic to the Late Cretaceous (Zhou and Li 2000; Zhou *et al*. 2006; Wang *et al*. 2011).

The Indosinian rocks (245–205 Ma) predominantly crop out as granitoids in the SCB, except for a few melanite-bearing pyroxene syenites and aegirite-augite-bearing syenites in Fujian Province (254–242 Ma) (Wang *et al*. 2005a) (Figure 1(b)) and rare alkali basalt (212–206 Ma) in Ningyuan, southern Hunan Province (Liu *et al*. 2010). In addition, mafic xenoliths in late Mesozoic basalts in Daoxian and Ningyuan, southern Hunan Province (Guo *et al*. 1997; Jiang *et al*. 2009; Liu *et al*. 2012), record Indosinian mafic magmatism in the lower continental crust (233–220 Ma), whereas the host magma was attributed to a depleted mantle source (Guo *et al*. 1997; Dai *et al*. 2008). The early Indosinian granitoids, accounting for about 40% of the Indosinian granitoids (Zhou *et al*. 2006), vary from metaluminous (A/CNK <1.0) biotite granites and granodiorites with or without hornblende and epidote to peraluminous (A/CNK >1.0) biotite monzogranite and granite with or without muscovite, garnet, tourmaline, and cordierite (HNGBMR 1988; Deng *et al*. 2004; Qiu *et al*. 2004; Zhang *et al*. 2004; Wang *et al*. 2007; Sun *et al*. 2010; Cao *et al*. 2011; Han *et al*. 2011). In comparison, the late Indosinian granitoids consist of weakly peraluminous (A/CNK = 1.0–1.1) biotite monzogranite and granite and strongly peraluminous (A/CNK >1.1) two-mica

monzogranite, with or without tourmaline and garnet (HNGBMR 1988; Sun *et al*. 2005; Chen *et al*. 2006, 2007a, 2007b; Ding *et al*. 2006; Wang *et al*. 2006; Wang *et al*. 2007). Most of the Indosinian granitoids show massive textures of coarse to medium grain size, except for some early Indosinian granitoids in Guangxi and Guangdong Provinces located close to the Ailaoshan–Red River suture, which show gneissic or mylonitized textures (HNGBMR 1988; Shao *et al*. 1995; Deng *et al*. 2004; Zhou *et al*. 2006). Indosinian peraluminous granitoids are considered on the basis of petrological observations to have been emplaced at a relatively shallow depth of 5–13 km (Zhou *et al*. 2006). A similar conclusion is reached by their position on a CIPW-normative Qz-Ab-Or diagram (Chen *et al*. 2007a; Wang *et al*. 2007).

The Weishan granitic pluton is situated in the joint region of Ningxiang, Shaoshan, Xiangxiang, and Anhua Counties, Hunan Province. It crops out over an area of around 1240 km^2, and is one of the largest granitic batholiths in Hunan Province (HNGBMR 1988). The pluton intruded into Neoproterozoic to Devonian strata and was overlain by Upper Cretaceous strata. Intrusive contacts are commonly sharp, but contact metamorphism is not prominent (Figure 2). Various isotopic dating methods, including mica K-Ar, whole-rock Rb-Sr, zircon U-Pb, and monazite U-Th-Pb, have previously been applied to the study of the Weishan pluton. The results revealed an age span ranging from 163 to 257 Ma (HNGBMR 1988; Ding *et al*. 2006; Wang *et al*. 2007).

The most common mineral assemblage of the Weishan pluton consists of plagioclase, K-feldspar, quartz, biotite, and muscovite, making up two series of granites (i.e. biotite and two-mica granitoids). Biotite granitoids, mainly located in Xinpu, Yueshanwan, Tangshi, and Qingshanqiao (Figure 2), make up about 60% of the pluton and include biotite granite, biotite monzogranite, hornblende-biotite monzogranite, and hornblende-biotite granodiorite of medium to fine grain size and porphyritic or granitic texture. Their major mineral assemblage is quartz (20–45%), K-feldspar (20–30%), plagioclase (An = 22–37, 30–35%), and biotite (5–10%). A few euhedral grains of hornblende (<1%), allanite, and epidote occur occasionally in the margin of the pluton. Two-mica granitoids are mainly characterized by medium- to fine-grained biotite and magmatic-derived muscovite, distributed in Xiangzikou, Yueshanwan, and Xinpu (Figure 2). Their major mineral assemblage is K-feldspar (30–40%), plagioclase (An = 5–38, 20–30%), quartz (15–30%), muscovite (3–10%), and biotite (±5%). Tourmaline is occasionally observed in the inner part of two-mica granitoids. Field relationships clearly show that the emplacement and crystallization of biotite granitic magmas occurred before two-mica granitic magmas (Figure 2).

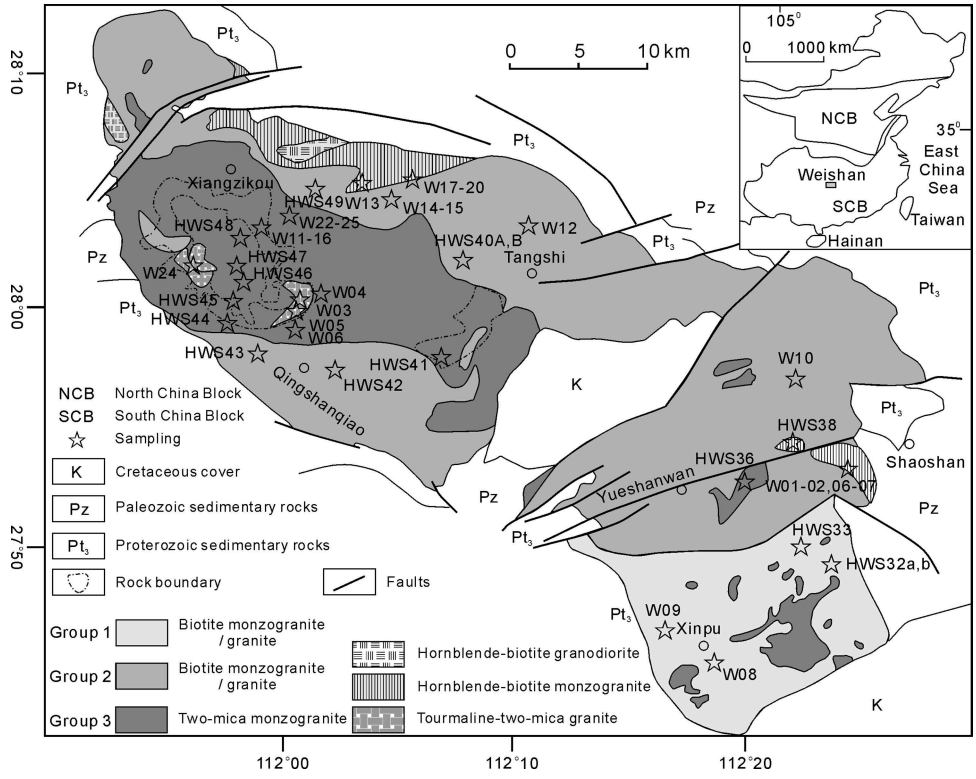

Figure 2. Geological simplified map of the Weishan granitoids, showing its multi-stage magmatism, modified after HNGBMR (1988).

3. Analytical methods

3.1. Single-grain mica Rb-Sr isochron dating

Biotite grains from the Xinpu biotite granite (HWS32b) and Qingshanqiao biotite monzogranite (HWS42) and muscovite grains from the Xiangzikou tourmaline two-mica granite (W03) were collected for Rb-Sr dating. Single biotite or muscovite grains were carefully chosen from 50-mesh-size fractions by handpicking under a binocular microscope and weighted using an ultra-microbalance. Chemical separation of Rb and Sr was performed at the Laboratory for Radiogenic Isotope Geochemistry (LRIG), Institute of Geology and Geophysics, Chinese Academy of Sciences, Beijing. Mica samples were rinsed in analysis-grade alcohol and then in weak HCl solution to eliminate contamination, and spiked with a mixed solution of ^{87}Rb-^{84}Sr (98%) tracers. The samples were dissolved with 2 ml HF and 0.2 ml HNO_3 at about 195°C for 48 h. After the samples were taken to dryness, 0.1 ml of 3 mol HNO_3 was added to the vessels. The samples were heated again, to convert fluorides to more soluble nitrates. Separation and purification of Rb and Sr were conducted on Teflon columns with about 0.1 ml Sr-Spec resin. Isotopic ratios of Rb and Sr were measured on an IsoProbe-T mass spectrometer at the Institute of Geology and Geophysics, Chinese Academy of Sciences. Sr was loaded with 1 μl 2 mol HNO_3 and 1 μl purified Ta-HF emitter solution onto a single W filament, and Rb was loaded with 1 μl 2 mol HNO_3 onto a single Ta filament. Sr isotopic ratios of samples were measured using the static Faraday multicollector mode, with simultaneous monitoring of ^{85}Rb by the Daly receiver to control isobaric interference of rubidium. Correction for mass fractionation of Sr isotopic ratios was based on $^{88}Sr/^{86}Sr = 8.37521$ using a power law. Internal precision of $^{87}Sr/^{86}Sr$ was better than 0.002% for measurement of 120 scans, with six seconds integration time per scan. During the analysis, NBS-987 Sr standard solution was used to monitor the stability of the instrument. The detailed chemical procedure and analytical conditions are described in Li *et al*. (2005). Uncertainty in regard to the $^{87}Sr/^{86}Sr$ ratios is expressed as 2σ precision of the measurement. A 2% uncertainty is assigned to the $^{87}Rb/^{86}Sr$ ratio, and a 0.005% uncertainty for the $^{87}Sr/^{86}Sr$ ratio is used as the error estimate for external precision. Age errors are quoted at the 95% confidence level. Data regression of isochrons and age calculations were performed by Isoplot 2.49a (Ludwig 1991).

3.2. Zircon U-Pb dating

Zircons for U-Pb dating were collected from the Yueshanwan two-mica monzogranite (HWS36), Tangshi biotite granite (HWS40), and Xiangzikou two-mica monzogranite (HWS41, HWS48, and W03), and separated using elution, magnetic, and conventional heavy liquid methods, following which more than 50 zircons for each sample were selected under a binocular microscope, mounted in epoxy, and polished to near half-section to expose their internal structures. Cathodoluminescent (CL) imaging to reveal the microstructure of the zircons was carried out on a Cameca electron microprobe at the Institute of Geology and Geophysics, Chinese Academy of Sciences. The analytical voltage and current for the CL was 50 kV and 15 nA. Except for sample W03, laser ablation ICP-MS (LA-ICP-MS) zircon U-Pb dating was carried out at the State Key Laboratory of Continental Dynamics, Northwest University, Xi'an. LA-ICP-MS is a combination of the GeoLas 200 M laser ablation system equipped with a 193 nm ArF-excimer laser and ICP-MS, which is an ELAN610DRC from Perkin Elmer/SCIEX (ON, Canada) with a dynamic reaction cell. Helium was used as the carrier gas to enhance the transport efficiency of the ablated material. The instrument was optimized via a NIST SRM 610 for maximum sensitivity, signal stability, minimum oxide/element ratios, and background. All measurements were performed using zircon TEM (417 Ma) for making isotopic fractionation corrections and zircon 91,500 (1064 Ma) as the external standard for age calculation. During the course of measurement, the signals for ^{206}Pb and ^{207}Pb were more than 20-fold higher than that of ^{204}Pb, which was very low and almost indistinguishable from the background, so no correction was made for common Pb. The operating processes and instrumental parameters are described in detail by Yuan *et al*. (2003). Isotopic ratios and U-Pb ages were calculated using GLITTER 4.0 (Macquarie University).

LA-ICP-MS zircon U-Pb dating for sample W03 was conducted at the State Key Laboratory of Isotope Geochemistry, Guangzhou Institute of Geochemistry, Chinese Academy of Sciences. The LA-ICP-MS system comprises an Agilent 7500a ICP-MS coupled with a Resonetic RESOLution M-50 ArF-Excimer laser source (λ = 193 nm). The operating conditions were 80 mJ laser energy and a repetition rate of 10 Hz, with a spot size of 31 μm diameter and 40 s ablation time (Liang *et al*. 2009). Helium was used as the carrier gas for the sample ablation aerosols to the ICP source. NIST610 and TEM were used as external calibration standards, and ^{29}Si as the internal standard (Li *et al*. 2012). The calculation of zircon isotope ratios and ages was performed by ICPMSDataCal 7.0 (Liu *et al*. 2008). All weighted mean age calculations and concordia diagram plots were carried out by Isoplot 2.49a (Ludwig 1991).

3.3. Biotite major elements and whole-rock major and trace elements

Mineral identification and major element analysis for biotite in thin sections were carried out on a JEOL JXA-8100

SuperProbe at the State Key Laboratory of Isotope Geochemistry, Guangzhou Institute of Geochemistry, Chinese Academy of Sciences, using an accelerating voltage of 15.0 kv, beam current of 10 nA, and spot diameter of 1 μm. Both silicates and pure oxides were used as standards.

Fresh samples were selected and powdered for major element, trace element, and isotope analyses. The major elements were determined by an ARL9800XP+ X-ray fluorescence (XRF) spectrometer at the Modern Analysis Centre of Nanjing University. The deviations of analysis relative to standard samples were less than 0.8% for high-concentration oxides and less than 10% for low-concentration oxides. Trace elements were determined by ICP-MS (Finnigan Element 2) at the State Key Laboratory of Mineral Deposit Research, Nanjing University. Detection limits were less than 0.5×10^{-9} and deviations of analysis relative to standard samples were less than 5%. Details of the analytical method can be found in Liang *et al*. (2000).

3.4. Sr-Nd isotope analyses

Sr-Nd isotopic compositions were determined using a MAT262 mass spectrometer at the Isotopic Laboratory, Institute of Geology and Geophysics, Chinese Academy of Sciences. Rb was monitored simultaneously during Sr measurement. All Sr data were corrected for mass fractionation based on $^{86}Sr/^{88}Sr = 0.1194$ and all Nd data based on $^{146}Nd/^{144}Nd = 0.7219$. The determined values of $^{87}Sr/^{86}Sr$ for the NBS987 and NBS607 standards were 0.710248 ± 12 (2σ) and 1.200241 ± 12 (2σ), respectively, and the values of $^{143}Nd/^{144}Nd$ for the BCR-1 and GBW04419 standards were 0.512602 ± 10 (2σ) and 0.512698 ± 13 (2σ), respectively. Analytical blanks were Sr (Rb) = 10^{-9}–10^{-10} g and Nd (Sm) = 5×10^{-11} g. The detailed description of this method can be found in Huang and Wu (1990).

4. Analytical results

4.1. Single mica Rb-Sr dating

Mica Rb-Sr isotopic compositions for the Weishan granite after correction for blank and spike are given in Table 1 and plotted in Figure 3, suggesting that the samples were formed in the Middle or Late Triassic. Both biotite and muscovite have high Rb concentrations (600–2010 ppm) compared with Sr (2.50–25.08 ppm), allowing for precise Rb-Sr ages. The isochron defined by four biotite grains from the Xinpu biotite granite HWS32b yields an age of 227.0 ± 13 Ma (MSWD = 1.6) (Figure 3(a)), and the isochron defined by six biotite grains from the Qingshanqiao biotite monzogranite HWS42 yields an age of 221.9 ± 5.8 Ma (MSWD = 3.8) (Figure 3(b)). Four muscovite grains from the Xiangzikou tourmaline two-mica granite yield an isochron age of 210.1 ± 3.3 Ma (MSWD = 0.21) (Figure 3(c)).

Table 1. Rb-Sr isotopic compositions for single mica grains.

Sample	No.	Mineral	Rb [μg/g]	Sr [μg/g]	$^{87}Rb/^{86}Sr$	$^{87}Sr/^{86}Sr$
HWS32b (Group 1)	1	Biotite	752.4	3.69	725.79	3.07534
	2		600.0	3.29	632.21	2.72514
	3		658.2	2.50	1001.35	3.92590
	4		894.4	3.92	831.33	3.36323
HWS42 (Group 2)	1	Biotite	1310.2	22.36	179.48	1.30538
	2		752.9	19.60	115.24	1.08498
	3		1408.8	7.82	623.59	2.72147
	4		1257.7	5.31	870.77	3.46531
	5		806.5	3.10	981.13	3.81327
	6		2010.3	18.59	346.01	1.79336
W03 (Group 3)	1	Muscovite	1506.8	6.64	813.20	3.15168
	2		1584.4	25.08	193.59	1.31001
	3		1524.5	6.29	885.36	3.38965
	4		1182.7	5.55	753.05	2.97839

4.2. LA-ICP-MS zircon U-Pb dating

The dating results for zircons from five representative granite samples of the Weishan pluton are listed in Table 2 and plotted in Figure 4.

4.2.1. Sample HWS36 (Yueshanwan two-mica monzogranite)

The zircons from this monzogranite are characteristically euhedral, up to 200 μm long, with length to width ratio of about 2:1. Euhedral concentric zoning is common in all crystals and a few inherited zircon cores can be observed. Fifteen analyses from this sample were made. In Figure 4(a) most of the analytical points are plotted on or near the concordia curve, indicating that the U-Pb systems have remained essentially closed. A few of the data points (e.g. HWS36-06 and HWS36-09) with relatively high $^{207}Pb/^{235}U$ values depart substantially from the concordia curve, a feature probably attributable to a high ^{207}Pb count during measurements. Because of this problem with the possibility of some interference at ^{207}Pb, the $^{206}Pb/^{238}U$ ages are considered more reliable. These range from 206 to 215 Ma, with the one exception of a Palaeozoic age (HWS36-20, 411 Ma) (Table 2, Figure 4(a)). The weighted mean age of 14 analyses is 211.0 ± 1.6 Ma (MSWD = 1.13), placing the time of crystallization in the Late Triassic.

4.2.2. Sample HWS40 (Tangshi biotite granite)

The zircons from this granite are euhedral, up to 300 μm long, with length to width ratio ranging from 3:1 to 2:1.

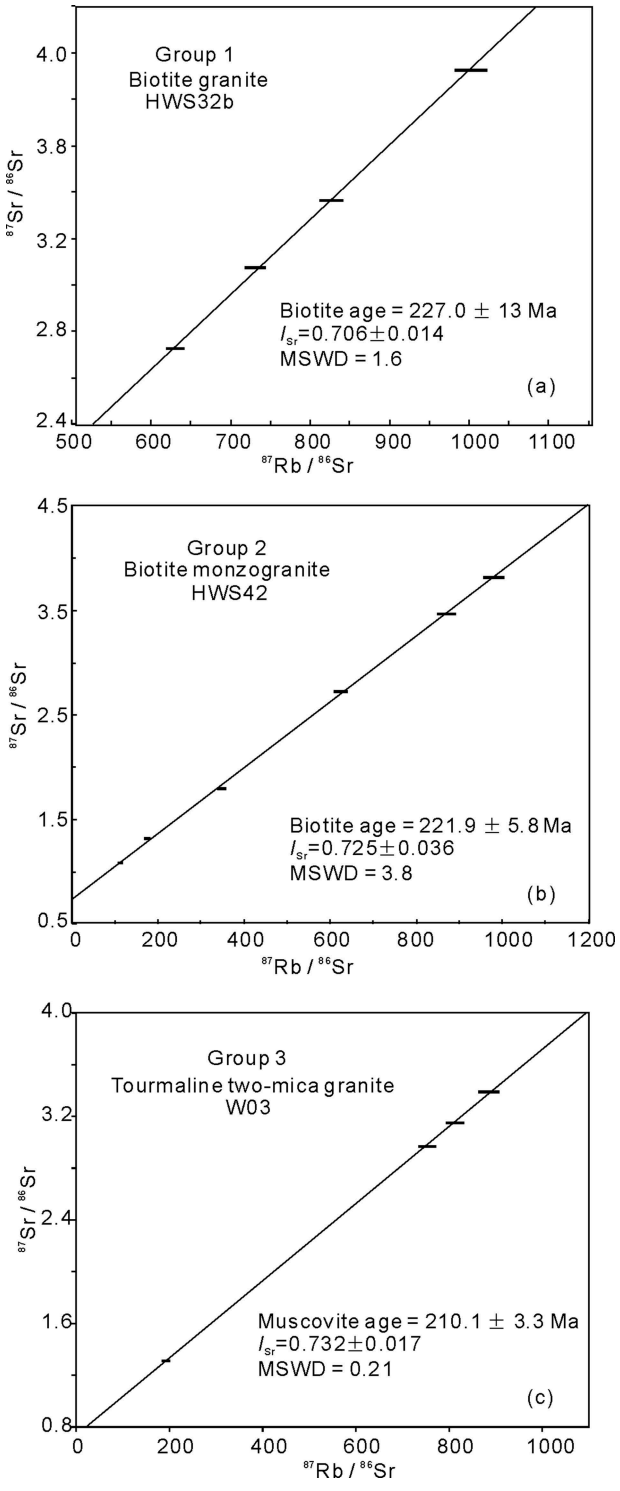

Figure 3. Single mica Rb-Sr isochron ages for biotite granite HWS32b (a), biotite monzogranite HWS42 (b), and tourmaline two-mica granite W03 (c).

Euhedral concentric zoning is common in all crystals, and a few inherited zircon cores can be observed. Thirteen zircons from sample HWS40 were analysed. In Figure 4(b), the analyses plot nearly co-linearly along the concordia curve, with ages ranging from 211 to 221 Ma (Table 2, Figure 4(b)). The weighted mean $^{206}Pb/^{238}U$ age is 215.7 ± 1.9 Ma (MSWD = 1.2) (Figure 4(b)), placing the time of crystallization in the Late Triassic.

4.2.3. *Sample HWS41 (Xiangzikou two-mica granite)*

The zircons from this granite are euhedral, up to 300 μm long, with length to width ratio varying from 3:1 to 2:1. Euhedral concentric zoning is common in all crystals, and a few inherited zircon cores can be observed. Fourteen zircons from sample HWS41 were analysed. It will be seen from Figure 4(c) that almost all the zircon analyses lie on or near the concordia curve, with the ages falling into two distinct clusters, ~220 and 181–196 Ma (Table 2, Figure 4(c)). When the points of analysis are located on the CL images, it is evident that the older Late Triassic ages, as represented by HWS41-20, were generally measured on the semi-round cores of crystals, while the younger ages, as represented by HWS41-09, were measured on igneous zircon overgrowths. The weighted mean age based on three analyses for the core is 221.5 ± 0.8 Ma (MSWD = 0.45), while that based on 11 analyses for the overgrowths is 187.4 ± 3.5 Ma (MSWD = 4.4), assigning it to the Early Jurassic.

4.2.4. *Sample HWS48 (Xiangzikou two-mica granite)*

The zircons from this granite are euhedral or subeuhedral, up to 300 μm long, with length to width ratio ranging from 3:1 to 1:1. Concentric zoning is common in most crystals, and many inherited zircon cores can be observed. Fourteen zircons from sample HWS48 were analysed. The majority of the analyses are discordant, with the other crystals yielding concordant ages (Figure 4(d)). The concordant ages vary from 180 to 188 Ma, with one exception being that of an old zircon dated at 855 Ma (HWS48-10). The discordant ages mostly range from 237 to 380 Ma (Table 2), with one exception being a very old age of 2358 Ma obtained from HWS48-06. Five of the concordant ages were determined on the magmatic overgrowths, yielding a weighted mean age of 184.5 ± 5.1 Ma (MSWD = 2.5) (Figure 4(d)), which, as with the overgrowths of sample HWS41, assigns it to the Early Jurassic.

4.2.5. *Sample W03 (Xiangzikou tourmaline two-mica granite)*

The zircons from this granite are euhedral, up to 200 μm long, with length to width ratio of about 2:1. Euhedral concentric zoning is common in all crystals, and a few inherited zircon cores can be observed. Thirty-nine analyses from the zircon rims (Table 2 and Figure 4(e)) and cores (Table 2 and Figure 4(f)) were carried out on sample W03. The ages obtained for the zircon rims vary from 201

Table 2. U-Th-Pb isotope data for zircons from Weishan granite in Hunan Province*.

	$^{207}Pb/^{235}U$		$^{206}Pb/^{238}U$		$^{207}Pb/^{206}Pb$		$^{208}Pb/^{232}Th$		$^{206}Pb/^{238}U$		$^{207}Pb/^{235}U$	
	ratio	1σ	ratio	1σ	ratio	1σ	ratio	1σ	age	1σ	age	1σ
HWS36 (Group 3)												
HWS36-01	0.21377	0.00817	0.03378	0.00049	0.04585	0.00177	0.00921	0.00019	214.2	3.06	196.7	6.83
HWS36-02	0.25995	0.00804	0.03330	0.00047	0.05656	0.00176	0.00926	0.00020	211.2	2.91	234.6	6.48
HWS36-03	0.21820	0.00793	0.03294	0.00048	0.04799	0.00176	0.00969	0.00021	208.9	2.97	200.4	6.61
HWS36-04	0.25981	0.00858	0.03249	0.00047	0.05795	0.00194	0.00857	0.00020	206.1	2.91	234.5	6.91
HWS36-06	0.48040	0.01051	0.03329	0.00045	0.10459	0.00231	0.01057	0.00012	211.1	2.81	398.3	7.21
HWS36-09	0.64146	0.01368	0.03304	0.00046	0.14074	0.00307	0.01017	0.00013	209.5	2.87	503.2	8.46
HWS36-12	0.29405	0.01189	0.03335	0.00052	0.06393	0.00264	0.00962	0.00027	211.5	3.24	261.7	9.33
HWS36-13	0.24507	0.00865	0.03341	0.00048	0.05319	0.00190	0.00898	0.00022	211.9	2.97	222.6	7.05
HWS36-14	0.22791	0.00891	0.03383	0.00049	0.04886	0.00194	0.00982	0.00028	214.5	3.07	208.5	7.37
HWS36-15	0.20848	0.00813	0.03360	0.00048	0.04501	0.00177	0.00843	0.00016	213.0	2.99	192.3	6.83
HWS36-16	0.20505	0.01385	0.03250	0.00060	0.04579	0.00315	0.01025	0.00039	206.1	3.73	189.4	11.67
HWS36-17	0.25860	0.00883	0.03430	0.00048	0.05472	0.00189	0.01077	0.00023	217.4	3.00	233.5	7.12
HWS36-18	0.24752	0.01001	0.03315	0.00049	0.05421	0.00223	0.01049	0.00025	210.2	3.08	224.6	8.15
HWS36-20	0.99724	0.04365	0.06579	0.00123	0.11007	0.00502	0.01344	0.00033	410.8	7.41	702.4	22.19
HWS36-21	0.22937	0.00952	0.03264	0.00048	0.05105	0.00215	0.00922	0.00029	207.0	3.01	209.7	7.86
HWS40 (Group 2)												
HWS40-01	0.23575	0.00763	0.03463	0.00046	0.04940	0.00162	0.00958	0.00025	219.4	2.89	214.9	6.27
HWS40-02	0.27983	0.00613	0.03344	0.00042	0.06073	0.00133	0.01048	0.00017	212.0	2.60	250.5	4.87
HWS40-03	0.38870	0.00987	0.03352	0.00045	0.08414	0.00218	0.01236	0.00021	212.5	2.81	333.4	7.22
HWS40-04	0.38538	0.01149	0.03353	0.00047	0.08339	0.00254	0.01127	0.00019	212.6	2.95	331.0	8.42
HWS40-05	0.28289	0.00644	0.03395	0.00042	0.06047	0.00138	0.01330	0.00020	215.2	2.63	252.9	5.10
HWS40-07	0.28208	0.00671	0.03486	0.00044	0.05871	0.00140	0.01247	0.00021	220.9	2.75	252.3	5.31
HWS40-08	0.28044	0.00806	0.03391	0.00045	0.06001	0.00175	0.01160	0.00022	215.0	2.83	251.0	6.39
HWS40-09	0.25829	0.00868	0.03449	0.00047	0.05433	0.00185	0.01114	0.00026	218.6	2.96	233.3	7.00
HWS40-10	0.49123	0.01368	0.03452	0.00050	0.10325	0.00297	0.02078	0.00041	218.8	3.10	405.7	9.32
HWS40-14	0.24781	0.00709	0.03420	0.00045	0.05257	0.00152	0.01083	0.00022	216.8	2.80	224.8	5.77
HWS40-17	0.49088	0.01371	0.03385	0.00049	0.10520	0.00303	0.01556	0.00027	214.6	3.05	405.5	9.33
HWS40-18	0.28822	0.00739	0.03333	0.00043	0.06272	0.00162	0.01270	0.00026	211.4	2.71	257.2	5.82
HWS40-21	0.23108	0.00795	0.03430	0.00047	0.04887	0.00170	0.01093	0.00029	217.4	2.92	211.1	6.56
HWS41 (Group 3)												
HWS41-01	0.24445	0.00737	0.03482	0.00046	0.05092	0.00155	0.00990	0.00023	220.7	2.87	222.1	6.02
HWS41-02	0.20789	0.00469	0.02910	0.00036	0.05181	0.00117	0.00378	0.00006	184.9	2.26	191.8	3.95
HWS41-03	0.26295	0.00720	0.03044	0.00040	0.06266	0.00174	0.01152	0.00024	193.3	2.52	237.0	5.79
HWS41-06	0.22746	0.00540	0.02862	0.00036	0.05766	0.00138	0.00719	0.00013	181.9	2.26	208.1	4.47
HWS41-08	0.19608	0.00941	0.02844	0.00045	0.05003	0.00245	0.00798	0.00028	180.8	2.82	181.8	7.99
HWS41-09	0.24338	0.00926	0.03062	0.00045	0.05768	0.00224	0.00742	0.00016	194.4	2.81	221.2	7.56
HWS41-10	0.22621	0.00801	0.02981	0.00042	0.05507	0.00199	0.00831	0.00015	189.4	2.64	207.1	6.63
HWS41-11	0.23620	0.00712	0.02964	0.00040	0.05782	0.00177	0.00522	0.00011	188.3	2.49	215.3	5.85
HWS41-14	0.25025	0.00718	0.02910	0.00039	0.06242	0.00182	0.00596	0.00010	184.9	2.44	226.8	5.83
HWS41-15	0.18844	0.00548	0.03092	0.00040	0.04424	0.00130	0.00863	0.00022	196.3	2.49	175.3	4.68
HWS41-16	0.22897	0.00924	0.03484	0.00050	0.04770	0.00196	0.00962	0.00032	220.8	3.14	209.4	7.63
HWS41-18	0.19870	0.00572	0.02867	0.00037	0.05031	0.00147	0.00558	0.00013	182.2	2.34	184.0	4.85
HWS41-19	0.21182	0.00823	0.02959	0.00043	0.05197	0.00206	0.00782	0.00021	188.0	2.68	195.1	6.90
HWS41-20	0.25557	0.00685	0.03521	0.00045	0.05269	0.00143	0.00665	0.00014	223.1	2.82	231.1	5.54
HWS48 (Group 3)												
HWS48-01	0.21368	0.01264	0.02840	0.00052	0.05468	0.00330	0.00869	0.00048	180.5	3.24	196.6	10.57
HWS48-02	0.20450	0.00630	0.02960	0.00040	0.05022	0.00155	0.00800	0.00051	188.0	2.50	188.9	5.31
HWS48-03	0.19542	0.01005	0.02944	0.00047	0.04824	0.00252	0.00780	0.00037	187.0	2.96	181.2	8.54
HWS48-04	0.23838	0.00603	0.02835	0.00037	0.06111	0.00154	0.00762	0.00016	180.2	2.32	217.1	4.94
HWS48-05	0.96773	0.03906	0.06073	0.00108	0.11580	0.00486	0.02812	0.00061	380.1	6.58	687.3	20.15
HWS48-06	7.20286	0.10217	0.34650	0.00430	0.15107	0.00201	0.08057	0.00104	1917.9	20.59	2136.9	12.65
HWS48-07	0.23684	0.00563	0.03598	0.00045	0.04784	0.00112	0.01004	0.00017	227.8	2.83	215.8	4.62
HWS48-08	0.19624	0.00597	0.02964	0.00039	0.04811	0.00147	0.00774	0.00022	188.3	2.47	181.9	5.06
HWS48-09	0.47657	0.01606	0.04351	0.00065	0.07960	0.00274	0.03574	0.00084	274.6	4.03	395.7	11.04
HWS48-10	1.28306	0.04377	0.14185	0.00208	0.06573	0.00227	0.03929	0.00089	855.1	11.74	838.2	19.47

(*Continued*)

Table 2. (Continued).

	$^{207}Pb/^{235}U$		$^{206}Pb/^{238}U$		$^{207}Pb/^{206}Pb$		$^{208}Pb/^{232}Th$		$^{206}Pb/^{238}U$		$^{207}Pb/^{235}U$	
	ratio	1σ	ratio	1σ	ratio	1σ	ratio	1σ	age	1σ	age	1σ
HWS48-11	0.32478	0.01072	0.03746	0.00053	0.06302	0.00211	0.01454	0.00070	237.0	3.32	285.6	8.22
HWS48-12	0.32042	0.00817	0.03992	0.00052	0.05834	0.00149	0.02257	0.00067	252.3	3.24	282.2	6.28
HWS48-13	0.39151	0.01319	0.04527	0.00065	0.06286	0.00214	0.02888	0.00107	285.4	3.99	335.5	9.62
HWS48-14	1.54759	0.06207	0.11386	0.00197	0.09878	0.00408	0.04055	0.00076	695.1	11.37	949.5	24.74
W03R (Group 3)												
W03-03	0.23633	0.00549	0.03317	0.00032	0.05119	0.00116	0.01270	0.00035	210.4	2.01	215.4	4.51
W03-08	0.28866	0.00882	0.03317	0.00029	0.06330	0.00214	0.01171	0.00031	210.4	1.79	257.5	6.95
W03-10	0.27618	0.00862	0.03058	0.00031	0.06512	0.00207	0.01034	0.00028	194.2	1.96	247.6	6.86
W03-11	0.26458	0.00672	0.03244	0.00028	0.05846	0.00149	0.01033	0.00026	205.8	1.73	238.4	5.39
W03-14	0.24347	0.00708	0.03327	0.00042	0.05230	0.00144	0.01163	0.00033	211.0	2.60	221.3	5.78
W03-15	0.30058	0.00933	0.03318	0.00035	0.06474	0.00202	0.00882	0.00024	210.4	2.20	266.9	7.29
W03-16	0.24806	0.00689	0.03351	0.00033	0.05289	0.00148	0.01118	0.00032	212.5	2.06	225.0	5.61
W03-18	0.24878	0.00687	0.03373	0.00038	0.05298	0.00144	0.01267	0.00033	213.8	2.37	225.6	5.58
W03-20	0.25562	0.00959	0.03253	0.00040	0.05597	0.00194	0.01058	0.00033	206.4	2.51	231.1	7.75
W03-21	0.22971	0.00669	0.03316	0.00028	0.04956	0.00147	0.01249	0.00032	210.3	1.72	210.0	5.53
W03-24	0.23098	0.00746	0.03259	0.00039	0.05034	0.00159	0.01144	0.00034	206.7	2.45	211.0	6.15
W03-25	0.29668	0.01013	0.03331	0.00039	0.06331	0.00218	0.01266	0.00039	211.2	2.41	263.8	7.94
W03-26	0.22121	0.00695	0.03388	0.00040	0.04637	0.00145	0.01094	0.00031	214.8	2.52	202.9	5.78
W03-27	0.40244	0.01353	0.03400	0.00039	0.08367	0.00269	0.00621	0.00035	215.5	2.41	343.4	9.80
W03-29	0.22984	0.00586	0.03196	0.00030	0.05129	0.00134	0.00980	0.00026	202.8	1.89	210.1	4.83
W03-30	0.24830	0.00706	0.03260	0.00034	0.05443	0.00160	0.01016	0.00027	206.8	2.11	225.2	5.74
W03-31	0.26993	0.00713	0.03164	0.00030	0.06101	0.00160	0.01319	0.00036	200.8	1.84	242.6	5.70
W03-33	0.27103	0.00847	0.03158	0.00032	0.06203	0.00204	0.00951	0.00031	200.5	2.01	243.5	6.77
W03-35	0.27337	0.00829	0.03200	0.00030	0.06141	0.00184	0.01030	0.00027	203.1	1.88	245.4	6.61
W03-36	0.27986	0.00789	0.03262	0.00035	0.06153	0.00170	0.01219	0.00033	207.0	2.18	250.5	6.26
W03-37	0.28841	0.00772	0.03390	0.00031	0.06089	0.00165	0.01037	0.00030	214.9	1.91	257.3	6.08
W03-38	0.24914	0.00750	0.03309	0.00045	0.05352	0.00152	0.01001	0.00029	209.8	2.83	225.9	6.09
W03-39	0.21258	0.00663	0.03239	0.00039	0.04658	0.00148	0.00970	0.00032	205.5	2.46	195.7	5.55
W03-40	0.22698	0.00838	0.03231	0.00044	0.04952	0.00183	0.01058	0.00038	205.0	2.74	207.7	6.93
W03C (Group 3)												
W03-01	0.28630	0.00869	0.03481	0.00042	0.05898	0.00172	0.01504	0.00047	220.6	2.64	255.6	6.86
W03-02	0.25262	0.00697	0.03443	0.00046	0.05257	0.00131	0.01139	0.00033	218.2	2.85	228.7	5.65
W03-05	0.46520	0.01899	0.03592	0.00041	0.09233	0.00354	0.01665	0.00061	227.5	2.54	387.9	13.16
W03-06	0.24641	0.00786	0.03435	0.00042	0.05169	0.00157	0.01189	0.00034	217.7	2.63	223.7	6.40
W03-07	0.38459	0.01723	0.03526	0.00042	0.07714	0.00288	0.01153	0.00030	223.4	2.63	330.4	12.64
W03-09	0.37687	0.01752	0.03538	0.00053	0.07393	0.00275	0.01176	0.00039	224.1	3.30	324.7	12.92
W03-12	0.31210	0.00992	0.03809	0.00050	0.05892	0.00182	0.01473	0.00046	241.0	3.10	275.8	7.68
W03-13	0.25048	0.00736	0.03478	0.00046	0.05162	0.00145	0.01010	0.00025	220.4	2.86	227.0	5.98
W03-17	0.26984	0.01106	0.03666	0.00054	0.05332	0.00216	0.01219	0.00043	232.1	3.33	242.6	8.85
W03-19	0.33296	0.01048	0.03456	0.00038	0.06913	0.00214	0.01189	0.00034	219.0	2.38	291.8	7.98
W03-22	0.25316	0.00746	0.03478	0.00039	0.05177	0.00143	0.01148	0.00034	220.4	2.42	229.1	6.04
W03-23	0.22867	0.00749	0.03454	0.00040	0.04728	0.00153	0.01100	0.00032	218.9	2.50	209.1	6.19
W03-28	0.49099	0.01747	0.03603	0.00046	0.09568	0.00299	0.03010	0.00124	228.2	2.87	405.6	11.90
W03-32	0.41095	0.01684	0.03437	0.00036	0.08451	0.00313	0.00954	0.00028	217.8	2.25	349.6	12.12
W03-34	0.53856	0.01852	0.03700	0.00041	0.10350	0.00315	0.01559	0.00050	234.2	2.54	437.5	12.22

Note: *The laser bean diameter is 31–40 μm.

to 216 Ma, with one exception being a slightly younger age of 194 Ma obtained from W03-10. Twenty-two analyses yield a weighted mean Late Triassic age for the rim of 207.9 ± 1.9 Ma (MSWD = 4.3) (Figure 4(e)). In contrast, the ages on the zircon cores mostly range from 218 to 224 Ma, with a weighted mean age of 219.8 ± 1.6 Ma (MSWD = 0.63) (Figure 4(f)), with one core having a slightly older concordant age of 232 Ma based on W03-17. Therefore, the span of $^{206}Pb/^{238}U$ ages on the cores ranges from the Middle to Late Triassic.

4.3. *Whole-rock major and trace elements*

The analytical results of major and trace elements of whole rocks are listed in Tables 3 and 4. According to their geochemical and mineralogical characteristics and

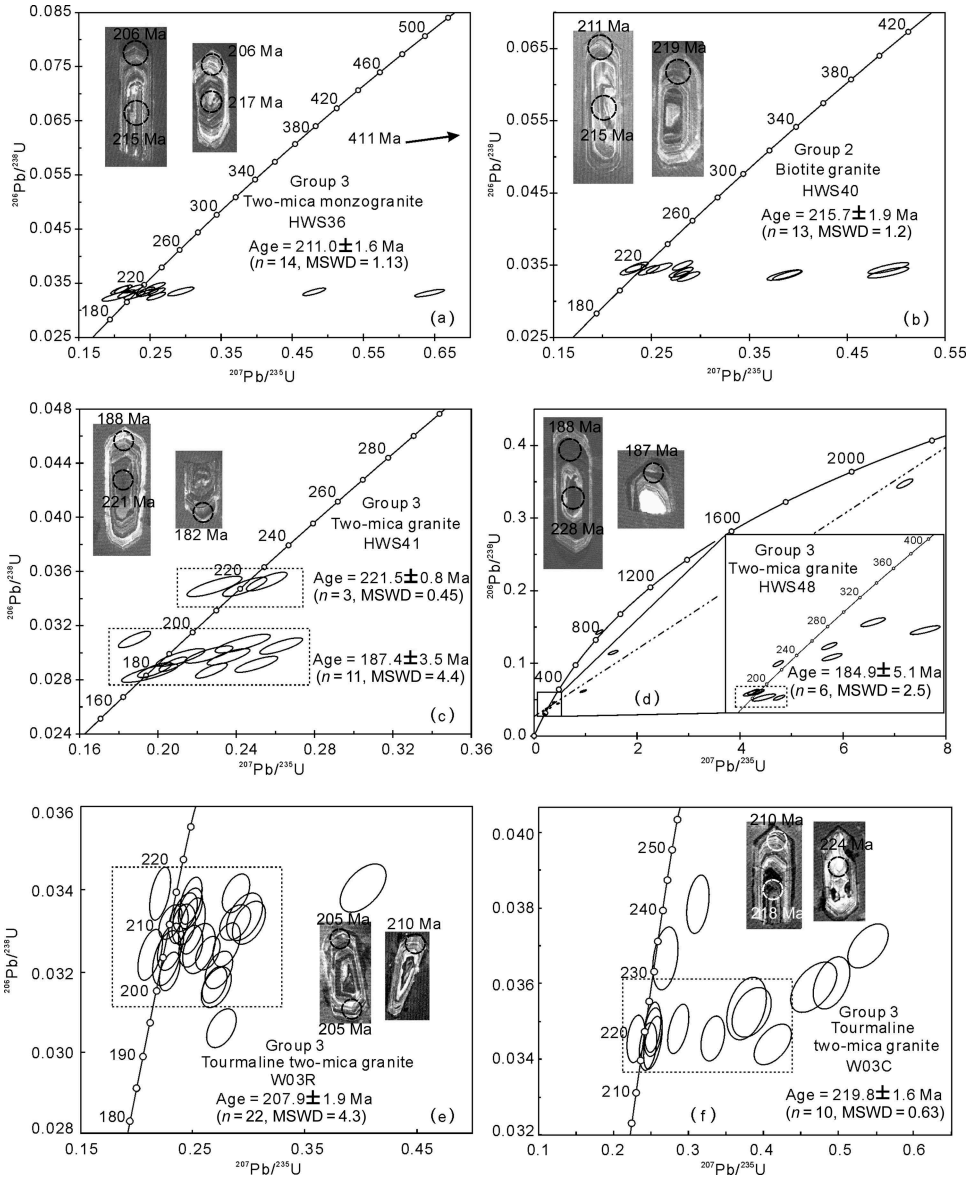

Figure 4. Zircon U-Pb concordia diagrams for the Weishan granites.

geocheonology, we divided the Weishan granites into three groups. Group 1 rocks, which crop out in Xinpu (Figure 2), plot entirely in the granite field of a Middlemost classification diagram in Figure 5(a). They have high SiO_2 (75.92–76.75%) and ALK (Na_2O + K_2O, 7.55–8.25%) and low MgO (0.10–0.29%), FeO (0.44–1.13%), CaO (0.67–0.94%), and TiO_2 (0.04–0.14%) – an extremely low solidification index (SI, 1.0–3.0) and intermediate ACNK values (1.04–1.08), indicating a weakly peraluminous composition (Figure 5(b)). Group 2 rocks crop out in Yueshanwan, Tangshi, and Qingshanqiaom, and plot mostly in the granodiorite and granite fields of a Middlemost classification diagram with an occasional sample plotting in the quartz monzogranite field in Figure 5(a). They have relatively high SI (3.0–19), variable ACNK values (0.94–1.52) (Figure 6(b)), and high FeO (1.51–3.83%) and MgO (0.37–1.93%). Group 3 rocks crop out in Xiangzikou, and plot totally in the granite field of a Middlemost classification diagram in Figure 5(a). They have moderately low SI (2.3–9.3) and high ACNK (1.05–1.20) (Figure 5(b)), together with high SiO_2 (70.51–75.37%) and Al_2O_3 (13.36–14.81%).

In the chemical variation diagram, all these rocks show high-K calc-alkaline affinities and a significant negative correlation between SiO_2 and Al_2O_3, TiO_2, MgO, CaO, and FeO^T, with Group 1 usually showing the lowest concentrations and Group 2 the highest (Figure 6). P_2O_5, on the other hand, is not obviously correlated with SiO_2 for any the groups (Figure 6(h)). Of the trace elements, Rb and Ta increase with SiO_2 from Group 2 to Group 3 to

Table 3. Major elements of Weishan pluton (wt.%).

	Group 1					Group 2								
Sample	HWS-32a Bi-Gr*	HWS-32b Bi-Gr	HWS-33 Bi-Gr	W08 Bi-Gr	W09 Bi-Gr	HWS-38 Amp-Bi-Gr	HWS-40A Bi-Gr	HWS-40B Bi-GD	HWS-42 Bi-MGr	HWS-43 Bi-MGr	HWS-49 Bi-Gr	W01 Bi-Gr	W02 Amp-Bi-MGr	W06 Bi-MGr
SiO_2	76.68	75.92	76.75	76.42	76.19	70.50	71.75	65.49	70.37	68.72	69.23	68.03	71.29	72.01
TiO_2	0.06	0.14	0.05	0.04	0.09	0.31	0.31	0.90	0.47	0.54	0.34	0.46	0.37	0.32
Al_2O_3	12.82	12.84	12.83	12.58	12.49	14.64	14.57	15.55	14.03	14.43	15.27	15.71	13.67	13.89
Fe_2O_3	0.18	0.32	0.39	1.10	0.29	0.77	0.34	1.26	0.79	0.81	0.87	0.53	1.18	0.16
FeO	0.77	1.13	0.44	0.61	1.05	1.87	2.08	3.48	2.65	3.33	1.69	3.12	2.83	2.11
MnO	0.10	0.06	0.03	0.04	0.04	0.06	0.04	0.08	0.06	0.08	0.05	0.07	0.08	0.07
MgO	0.10	0.25	0.09	0.29	0.15	0.71	0.83	1.43	1.22	1.40	0.85	1.26	0.81	0.74
CaO	0.94	0.91	0.67	0.93	0.78	1.56	2.14	3.34	2.43	2.46	0.97	2.97	2.52	2.05
Na_2O	3.34	3.23	3.52	3.23	3.43	3.23	3.11	3.02	3.01	3.17	1.77	3.48	3.08	3.10
K_2O	4.77	4.75	4.73	4.35	4.12	5.31	4.42	4.35	4.10	3.88	4.99	2.87	3.74	4.45
P_2O_5	0.04	0.06	0.04	0.04	0.03	0.10	0.12	0.34	0.16	0.17	0.12	0.16	0.10	0.11
LOI	0.23	0.40	0.53	0.39	0.61	0.86	0.39	0.79	0.46	0.61	3.70	0.77	0.46	0.39
Total	99.98	100.01	100.07	100.01	99.27	99.92	100.11	100.03	99.76	99.60	99.85	99.43	100.16	99.39
ALK	8.11	7.98	8.25	7.58	7.55	8.54	7.53	7.37	7.11	7.05	6.76	6.35	6.82	7.55
A/CNK	1.04	1.06	1.06	1.07	1.08	1.05	1.06	0.99	1.02	1.04	1.52	1.10	1.00	1.02
A/NK	1.20	1.23	1.18	1.26	1.24	1.32	1.47	1.61	1.49	1.53	1.84	1.78	1.50	1.40
Mg#	0.16	0.24	0.17	0.25	0.17	0.33	0.39	0.36	0.40	0.38	0.38	0.39	0.27	0.37
CaO/ Na_2O	0.28	0.28	0.19	0.29	0.23	0.48	0.69	1.11	0.81	0.78	0.55	0.85	0.82	0.66
Al_2O_3/ TiO_2	200	95	267	315	139	47	46	17	30	27	45	34	37	43
SI	1.09	2.58	0.98	3.03	1.66	5.97	7.70	10.56	10.37	11.12	8.36	11.19	6.96	7.01

(*Continued*)

Table 3. (Continued).

	Group 2													Group 3
Sample	W07 Amp-Bi-MGr	W10 Bi-MGr	W12 Bi-GD	W13 Amp-MGr	W14 Bi-MGr	W15 Bi-Gr	W17 Amp-Bi-GD	W18 Bi-MGr	W19 Amp-Bi-MGr	W20 Bi-MGr	W03-1 Amp-Bi-GD	W04-1 Bi-MGr	W05-1 Bi-Gr	HWS-44 Mus-Bi-Gr
SiO_2	68.80	70.42	67.96	70.31	67.77	70.02	66.96	66.74	69.43	70.12	66.31	68.34	72.22	72.18
TiO_2	0.29	0.32	0.58	0.37	0.59	0.33	0.68	0.31	0.56	0.32	0.66	0.52	0.25	0.23
Al_2O_3	14.71	15.08	14.31	14.53	13.98	14.53	14.99	16.90	14.26	14.16	15.47	15.12	14.26	14.74
Fe_2O_3	1.38	0.68	1.18	1.31	2.08	0.44	1.13	0.18	0.58	0.52	0.99	0.72	0.73	0.43
FeO	2.11	1.51	3.50	2.34	3.35	2.59	3.38	2.12	3.70	2.67	3.83	3.18	2.00	1.63
MnO	0.04	0.04	0.08	0.07	0.11	0.06	0.09	0.02	0.06	0.03	0.06	0.06	0.03	0.05
MgO	1.60	1.93	1.08	0.79	1.25	0.72	1.69	0.37	1.03	0.70	1.52	1.33	0.57	0.58
CaO	2.96	2.73	2.20	2.62	3.10	2.22	2.68	2.31	2.41	2.27	3.14	2.96	1.60	1.67
Na_2O	3.30	3.51	3.61	3.31	2.77	3.73	3.02	3.45	3.20	2.97	3.42	3.35	3.26	3.16
K_2O	4.49	2.56	3.61	3.74	3.42	3.54	4.26	6.09	4.05	4.85	3.61	3.81	4.53	4.74
P_2O_5	0.71	0.03	0.13	0.12	0.15	0.05	0.09	0.48	0.48	0.13	0.58	0.76	0.62	0.13
LOI	0.15	0.97	0.86	0.50	1.14	0.87	0.70	0.59	0.17	0.35	0.19	0.31	0.25	0.13
Total	99.77	99.78	100.09	100.01	99.70	99.09	99.67	100.15	99.93	99.03	99.78	100.46	100.32	100.09
ALK	7.79	6.07	7.22	7.05	6.19	7.27	7.28	9.54	7.25	7.82	7.03	7.16	7.79	7.90
A/CNK	0.94	1.12	1.03	1.02	1.01	1.04	1.04	1.03	1.02	0.99	1.01	1.01	1.08	1.10
A/NK	1.43	1.76	1.45	1.53	1.69	1.46	1.56	1.38	1.48	1.40	1.62	1.57	1.39	1.43
Mg#	0.46	0.62	0.30	0.29	0.30	0.30	0.41	0.23	0.31	0.29	0.37	0.38	0.28	0.34
CaO/ Na_2O	0.90	0.78	0.61	0.79	1.12	0.60	0.89	0.67	0.75	0.76	0.92	0.88	0.49	0.53
Al_2O_3/ TiO_2	50	47	25	39	24	44	22	55	25	44	23	29	57	64
SI	12.42	18.94	8.32	6.88	9.71	6.53	12.54	3.03	8.20	5.98	11.37	10.73	5.14	5.50

(*Continued*)

Table 3. (Continued).

	Group 3												
Sample	HWS-45 Mus-Bi-MGr	HWS-46 Mus-Bi-Gr	HWS-47 Mus-Bi-Gr	W03 Tur-Mus-Bi-Gr	W04 Mus-Bi-Gr	W05-2 Tur-Mus-Bi-Gr	W11 Mus-Bi-MGr	W16 Mus-Bi-Gr	W22 Mus-Bi-Gr	W23 Mus-Bi-MGr	W24 Tur-Bi-Gr	W25 Mus-Bi-MGr	W06 Mus-Bi-Gr
SiO_2	70.51	72.88	72.61	75.37	72.31	72.86	73.07	71.56	72.22	73.98	72.58	71.80	73.53
TiO_2	0.32	0.18	0.21	0.15	0.23	0.20	0.15	0.22	0.25	0.16	0.13	0.24	0.15
Al_2O_3	14.76	14.30	14.81	13.43	14.55	14.22	14.04	14.57	14.26	13.36	14.32	14.49	14.10
Fe_2O_3	0.67	0.31	0.19	0.20	0.18	0.06	0.06	0.20	0.73	1.37	0.79	0.32	0.24
FeO	1.93	1.25	1.51	1.32	2.32	2.10	1.43	2.14	2.00	1.64	1.90	2.60	1.41
MnO	0.06	0.04	0.04	0.04	0.04	0.03	0.03	0.04	0.03	0.02	0.05	0.06	0.04
MgO	0.68	0.45	0.52	0.47	0.66	0.50	0.41	0.25	0.57	0.25	0.61	0.94	0.37
CaO	1.55	1.51	2.06	1.13	1.56	1.70	2.20	1.57	1.60	0.90	1.59	2.11	0.93
Na_2O	3.18	3.04	3.14	2.99	2.64	2.99	2.98	3.37	3.26	2.63	3.23	3.25	3.26
K_2O	5.32	5.15	4.16	4.41	4.91	4.15	4.10	3.74	4.53	4.78	3.50	3.05	4.82
P_2O_5	0.10	0.12	0.13	0.11	0.12	0.12	0.11	0.03	0.62	0.45	0.58	0.35	0.76
LOI	0.82	0.58	0.56	0.54	0.55	0.66	0.52	0.86	0.25	0.28	0.30	0.27	0.21
Total	99.89	99.81	99.94	100.16	100.07	99.59	100.11	98.75	100.32	99.82	99.58	99.48	99.83
ALK	8.50	8.19	7.30	7.40	7.55	7.14	7.08	7.11	7.79	7.41	6.73	6.30	8.08
A/CNK	1.07	1.07	1.10	1.14	1.16	1.14	1.05	1.17	1.08	1.20	1.19	1.16	1.15
A/NK	1.34	1.35	1.53	1.39	1.51	1.51	1.65	1.52	1.39	1.41	1.57	1.68	1.33
Mg#	0.33	0.35	0.36	0.36	0.32	0.29	0.33	0.16	0.28	0.14	0.30	0.37	0.29
CaO/ Na_2O	0.49	0.50	0.66	0.38	0.59	0.57	0.74	0.47	0.49	0.34	0.49	0.65	0.29
Al_2O_3/ TiO_2	47	78	71	90	63	71	91	66	57	84	110	60	94
SI	5.77	4.41	5.46	5.01	6.16	5.10	4.57	2.58	5.14	2.34	6.08	9.25	3.66

Note: *Abbr. for granites: Bi, biotite; Amp, amphibole; Mus, musovite; Tur, tourmaline; Gr, granite; MGr, monzogranite; GD, granodiorite; Mg# = molar MgO/(MgO + FeO total); SI = 100 w (MgO)/(w(MgO) + w(Fe_2O_3) + w (FeO) + w(Na_2O) + w(K_2O)).

Table 4. Trace element analyses for Weishan granites.

	Group 1			Group 2							Group 3						
Sample	HWS32a	HWS32b	HWS-33	HWS-38	HWS-40A	HWS-40B	HWS-42	HWS-43	HWS-49	W01	HWS-44	HWS-45	HWS-46	HWS-47	W03	W04	W05-2
Ba	18.9	69.4	9.2	335	347	757	309	288	376	295	285	297	290	381	142	272	421
Rb	336	360	414	258	283	226	250	289	274	213	291	301	278	271	335	364	302
Sr	16.0	23.0	10.8	83.0	104	194	109	99.3	67.3	147	79.1	62.3	81.2	96.3	49.2	82.0	109
Y	32.4	49.5	37.0	27.0	27.8	31.2	24.3	28.9	14.8	20.2	10.0	12.9	11.9	8.35	19.0	14.2	11.3
Zr	75.9	107	62.0	181	160	320	235	251	153	190	102	148	108	128	68.9	108	119
Nb	10.8	12.6	13.6	11.8	14.3	24.6	14.6	18.9	13.1	13.5	13.8	11.5	10.7	10.2	13.7	14.1	13.0
Th	29.1	28.0	32.8	48.1	26.1	29.2	27.2	51.5	28.3	9.77	20.6	22.8	16.1	17.9	17.9	21.8	21.4
Pb	63.8	61.6	51.6	45.3	51.6	33.9	38.1	35.5	49.6	33.1	47.2	45.5	48.3	35.7	46.7	49.5	42.1
Ga	13.2	14.9	13.5	16.1	16.9	18.4	17.3	18.9	17.8	21.4	17.1	17.3	15.7	16.0	17.2	20.0	19.4
V	2.44	9.45	1.8	24.7	31.1	64.0	42.1	45.2	30.7	45.2	20.6	26.0	14.9	16.3	12.3	21.3	18.6
Cr	9.0	7.4	9.4	18.8	25.3	18.0	48.1	36.5	17.6	20.7	23.7	23.3	15.1	12.2	3.3	14.8	11.9
Hf	2.8	3.7	2.7	4.5	4.1	6.9	5.4	5.8	3.7	6.1	2.6	3.6	2.9	3.1	3.0	3.3	4.0
Cs	42.0	62.0	33.0	18.1	33.5	21.1	35.1	50.0	28.4	15.4	44.5	32.7	28.1	46.8	69.4	50.0	43.0
Sc	2.5	3.9	1.7	6.7	6.0	10.2	8.2	8.8	6.2	10.2	5.0	5.2	3.5	3.3	5.3	8.3	5.7
Ta	3.0	3.3	4.9	1.8	2.5	2.2	2.1	3.2	2.1	1.5	2.9	2.4	2.1	2.3	3.7	1.9	2.0
Co	0.9	1.6	0.4	4.2	5.5	11.2	7.9	8.9	6.8	8.1	3.8	4.9	2.9	3.0	2.5	3.7	3.7
Li	134	122	78.5	81.3	121	129	104	138	105	94	137	137	104	128	195	212	183
U	16.0	16.8	15.2	7.6	8.8	6.2	7.8	8.6	6.1	5.6	4.5	5.4	4.9	12.3	5.5	15.8	4.1
W	2.4	3.8	1.6	1.3	0.8	1.2	2.4	1.3	0.7	1.4	1.5	1.5	1.7	1.1	1.2	2.7	2.0
Sn	11.8	17.4	10.6	9.7	15.2	7.6	10.7	11.6	11.7	7.4	17.7	13.8	13.4	12.2	16.7	18.0	14.7
Mo	0.8	0.6	1.4	1.4	1.3	1.4	3.4	1.6	0.6	0.6	1.6	0.8	0.9	0.7	0.1	0.7	0.6
Bi	2.1	3.2	5.9	1.5	0.8	1.2	2.0	1.6	2.0		3.6	3.0	1.7	2.3			
Ti	332	690	236	1723	1807	4979	2602	2899	1910	2877	1225	1421	962	1161	935	1450	1343
La	8.6	16.6	7.5	44.7	36.9	71.4	44.4	49.6	34.1	16.1	27.6	30.4	22.5	28.3	18.3	22.4	30.0
Ce	20.3	29.7	8.4	91.6	73.8	131	85.0	97.3	66.4	30.9	55.9	60.6	44.9	51.9	37.9	45.8	56.3
Pr	2.6	4.7	2.6	9.8	7.9	13.8	8.9	10.2	7.3	3.6	6.0	6.3	4.9	5.2	4.3	5.3	6.2
Nd	10.6	18.2	10.7	34.9	28.2	48.5	30.3	37.0	24.9	13.9	21.2	21.4	17.4	17.2	15.2	18.8	21.9
Sm	3.4	5.7	3.8	7.1	5.7	8.5	5.8	7.1	4.6	3.6	4.3	4.2	3.7	3.1	3.7	4.9	4.4
Eu	0.2	0.3	0.1	0.7	0.7	1.4	0.7	0.7	0.6	0.9	0.5	0.5	0.5	0.5	0.4	0.5	0.6
Gd	3.8	6.3	4.2	6.4	5.2	7.6	5.3	6.6	4.0	3.3	3.5	3.4	3.1	2.7	3.1	3.4	3.2
Tb	0.7	1.1	0.7	0.8	0.7	0.9	0.7	0.8	0.5	0.7	0.4	0.4	0.4	0.3	0.6	0.6	0.5
Dy	5.1	8.3	5.7	5.0	5.2	5.9	4.5	5.3	2.8	4.2	2.3	2.5	2.4	1.7	3.7	3.0	2.6
Ho	1.2	1.9	1.3	1.0	1.1	1.2	0.9	1.1	0.5	0.7	0.4	0.5	0.4	0.3	0.7	0.4	0.4
Er	3.6	5.6	4.1	2.8	3.1	3.4	2.6	3.0	1.5	2.1	1.0	1.5	1.2	0.9	1.8	1.4	1.0
Tm	0.6	0.9	0.7	0.4	0.4	0.4	0.3	0.4	0.2	0.3	0.1	0.2	0.2	0.1	0.3	0.2	0.1
Yb	3.5	5.4	4.5	2.3	2.6	2.7	2.1	2.5	1.4	2.1	0.8	1.3	1.0	0.7	2.1	1.3	1.0
Lu	0.6	0.9	0.7	0.4	0.4	0.4	0.3	0.4	0.2	0.3	0.1	0.2	0.2	0.1	0.3	0.2	0.1

(*Continued*)

Table 4. (Continued).

	Group 1			Group 2							Group 3						
Sample	HWS32a	HWS32b	HWS-33	HWS-38	HWS-40A	HWS-40B	HWS-42	HWS-43	HWS-49	W01	HWS-44	HWS-45	HWS-46	HWS-47	W03	W04	W05-2
LREE/HREE	2.4	2.5	1.5	10.0	8.2	12.2	10.5	10.0	12.5	5.0	13.4	12.4	10.6	15.3	6.4	9.4	13.3
(La/Yb)N	1.6	2.0	1.1	12.8	9.3	17.8	14.0	13.3	16.7	5.1	22.0	15.5	14.3	25.5	5.9	11.0	19.4
(La/Sm)N	1.5	1.8	1.2	3.9	4.0	5.1	4.7	4.2	4.5	2.7	3.9	4.5	3.7	5.5	3.0	2.8	4.2
(Gd/Yb)N	0.9	0.9	0.8	2.2	1.6	2.3	2.0	2.1	2.4	1.3	3.4	2.1	2.4	3.0	1.2	2.0	2.5
Eu/Eu*	0.2	0.1	0.1	0.3	0.4	0.5	0.4	0.3	0.4	0.8	0.4	0.4	0.5	0.5	0.3	0.4	0.5
Rb/Ba	17.8	5.2	44.8	0.8	0.8	0.3	0.8	1.0	0.7	0.7	1.0	1.0	1.0	0.7	2.4	1.3	0.7
Rb/Sr	20.9	15.7	38.3	3.1	2.7	1.2	2.3	2.9	4.1	1.5	3.7	4.8	3.4	2.8	6.8	4.5	2.8
La/Sm	2.5	2.9	2.0	6.3	6.5	8.4	7.7	7.0	7.4	4.4	6.4	7.3	6.1	9.1	5.0	4.6	6.8
La/Yb	2.5	3.0	1.7	19.3	14.2	26.9	21.2	20.1	25.3	7.8	33.3	23.5	21.6	38.5	8.9	16.7	29.4
Sr/Yb	4.6	4.2	2.4	35.9	39.7	73.1	52.1	40.3	50.0	71.1	95.4	48.2	78.0	131.1	23.9	61.2	106.5

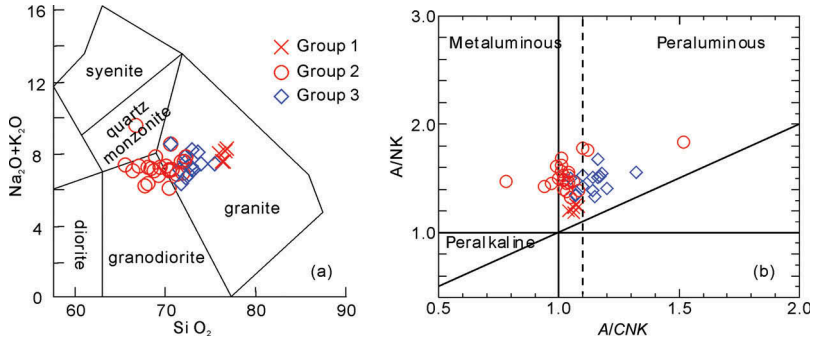

Figure 5. (a) Classification diagram for granitoids (Middlemost, 1994) (b) A/NK *versus* A/CNK for the Weishan granites. $A = Al_2O_3$, $N = Na_2O$, $K = K_2O$, $C = CaO$ (all in molar proportion).

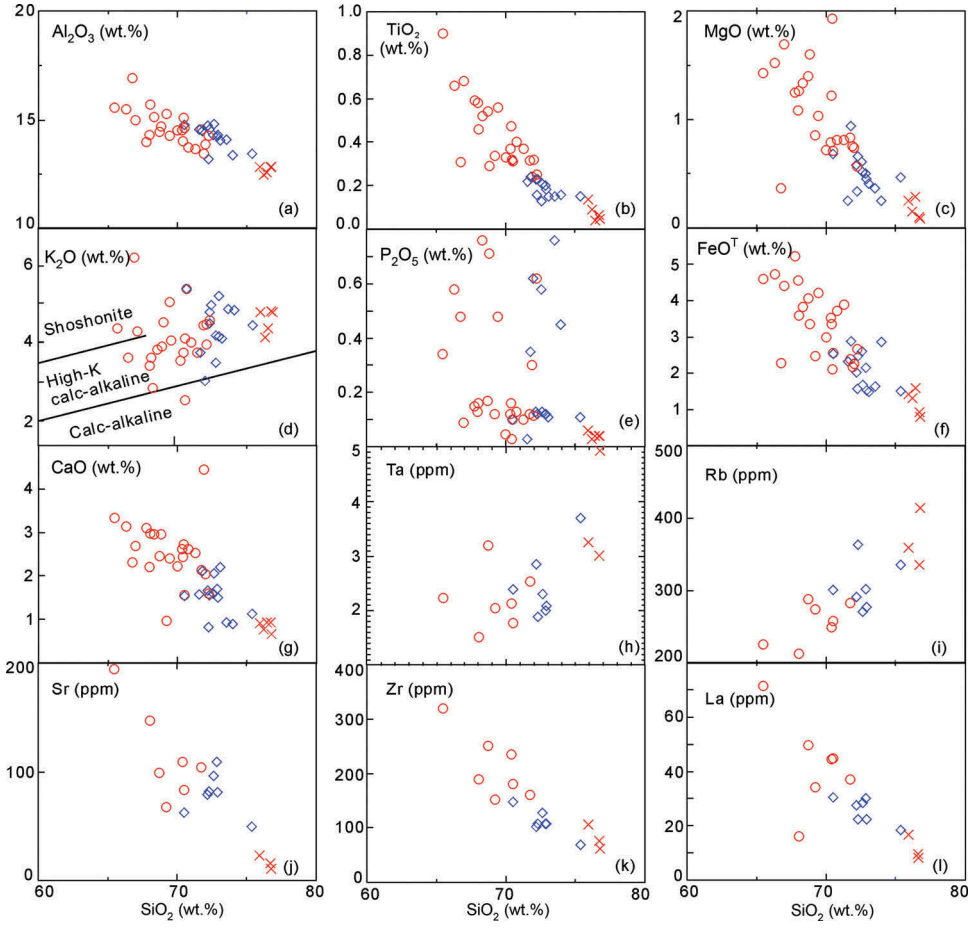

Figure 6. Chemical variation diagrams for the Weishan granites. Symbols are as in Figure 5.

Group 1, whereas Sr, Zr and La show an opposite tendency (Figure 6(h)–(l)).

Chondrite-normalized REE patterns are shown in Figure 7(a). Group 1 rocks display relatively flat REE patterns ($(La/Yb)_n$ = 1.11–2.01) whereas the other two groups have distinct light REE enrichments ($(La/Yb)_n$ = 5.14–19.4). All the samples have total REE contents of 92.2–329 ppm, and display moderate to high LREE enrichments, with ΣLREE/ΣHREE = 1.5–15.3. They show prominently negative Eu anomalies (Eu/Eu* = 0.09–0.54) and moderate HREE fractionation with $(Gd/Yb)_n$ = 0.75–3.43. Group 1 rocks have the most significant negative Eu anomalies and most fractionated HREE, with the lowest LREE but highest HREE concentrations, which induces ΣLREE/ΣHREE ratios (1.5–2.4) lower than those of other groups. On the MORB-normalized spidergram (Figure 7(b)), all the rock samples

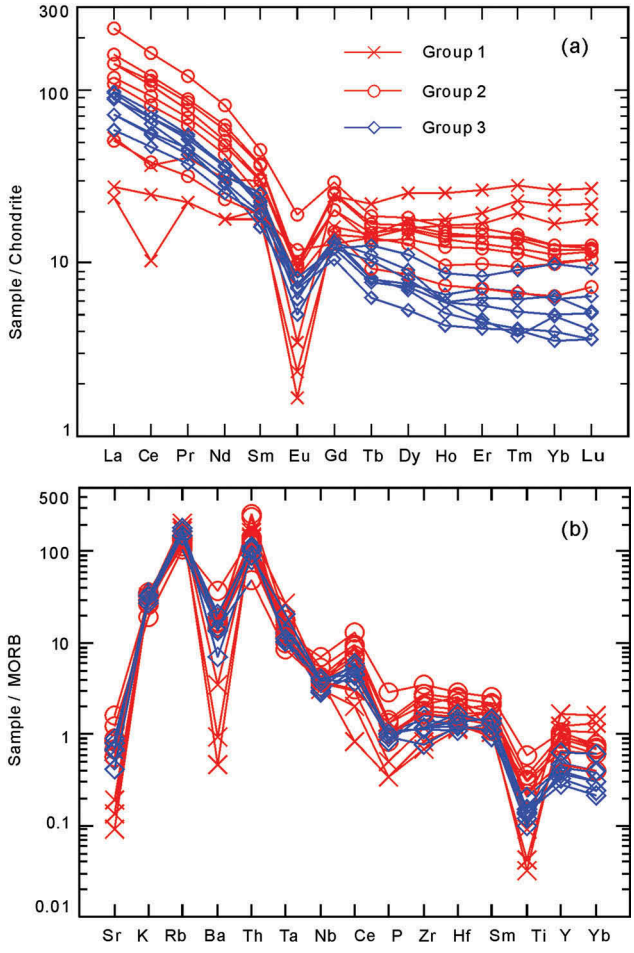

Figure 7. Chondrite-normalized REE diagrams and MORB-normalized trace element spidergram for the Weishan granites. Chondrite and MORB values are from Sun and McDonough (1989) and Pearce (1983), respectively.

exhibit obviously negative Ba, Sr, Nb, P, and Ti anomalies, with Group 1 displaying the most negative.

4.4. Biotite geochemical components

In order to investigate petrogenetic relationships, we analysed the compositions of representative biotites from each of the three groups. The analytical results are listed in Table 5. Biotites from the Weishan granitoids have 12.6–20.1% Al_2O_3, 15.8–25.8% FeO^T, 3.9–8.7% MgO, and 0.3–1.6% MnO. In the annite-siderophyllite-phlogopite-eastonite quadrilateral (Figure 8(a)), biotites from Group 1 are characterized by the highest Fe/(Fe + Mg) values and moderate total Al contents, whereas biotites from Group 3 have the highest total Al contents and those from Group 2 show the lowest total Al contents. In Figure 8(b), a Fe/(Fe + Mg) negative relationship with the SI can be observed, where decreasing solidification indices in the order Group 2 > Group 3 > Group 1 is similar to the tendency of the whole rocks.

4.5. Sr-Nd isotopic compositions

The $^{87}Sr/^{86}Sr$ and $^{143}Nd/^{144}Nd$ and the analytical errors are reported in Table 6 and shown in Figure 9. Group 2 rocks have initial $^{87}Sr/^{86}Sr$ ranging from 0.71003 to 0.71516 and $\varepsilon_{Nd}(t)$ values varying from –9.1 to –11.3, and T_{DM} modal ages of 1.75–1.90 Ga. One Group 3 sample exhibits a higher initial $^{87}Sr/^{86}Sr$ (0.72377), a lower $\varepsilon_{Nd}(t)$ value (–11.8), and a slightly higher T_{DM} model age (1.94 Ga). Both groups lie near or within the isotopic ranges of other Indosinian granites in Hunan Province (Figure 9).

5. Discussions

5.1. Petrogenesis

5.1.1. Emplacement time of major magmas

Our results from single-grain mica Rb-Sr isochron ages and LA-ICP-MS zircon U-Pb dating show that the Weishan pluton is the product of episodic magmatism in the Triassic- Early Jurassic. As representative of the Weishan pluton, Group 2 rocks, Qingshanqiao and Tangshi biotite granites, were formed at 221.9 ± 5.8 Ma and 215.7 ± 1.9 Ma, respectively. The Group 3 rocks, Yueshanwan two-mica granite, were emplaced at 211.0 ± 1.8 Ma and Xiangzikou two-mica granite was emplaced during at least two stages, in the Late Triassic (210.1 ± 3.3 Ma – 207.9 ± 1.9 Ma) and in the Early Jurassic (187.4 ± 3.5 Ma – 184.9 ± 5.1 Ma). The field relationships clearly show that circular contacts occur in the inner part of the Xiangzikou granite (Figure 2) (HNGBMR 1988), suggesting discrete pulses of magma. As for the age of Group 1 rocks, biotite Rb-Sr isochron dating indicates that the Xinpu biotite granite formed at 227.0 ± 13 Ma, significantly younger than the SHRIMP zircon U-Pb age of 243 ± 4 Ma (Wang *et al*. 2007). However, the Xinpu biotite granite displays extremely low SI values, a flat REE pattern, and strongly negative Eu, Ba, Sr, and Ti anomalies (Figure 7), analogous to those observed in highly fractionated granites (Chappell 1999; Jahn *et al*. 2001; Wu *et al*. 2003). As shown in Figure 10, the Xinpu biotite granite plots in the field of highly fractionated calc-alkaline rocks, distinguishable from other granites. Given that precursor magma to highly fractionated granite usually has experienced significant crystal fractionation and slow cooling (Chappell 1999; Wu *et al*. 2003), its biotite Rb-Sr age could be much younger than its zircon U-Pb age because of the lower closure temperature for this isotope system (Jenkin *et al*. 2001). That biotite-whole-rock/K-feldspar isochron ages are 18–25 million years younger than zircon U-Pb ages

Table 5. Average chemical compositions of biotite from Weishan complex granitic rocks (%).

Sample	HWS32a (Group 1)	HWS32b (Group 1)	HWS38 (Group 2)	HWS40 (Group 2)	HWS42 (Group 2)	HWS44 (Group 3)	HWS46 (Group 3)
Number	7	5	4	3	10	20	6
SiO_2	35.48	36.17	35.41	36.27	35.47	34.01	35.08
TiO_2	3.03	3.60	1.46	2.60	3.46	2.55	3.76
Al_2O_3	15.01	14.15	17.40	15.40	13.57	18.60	19.41
Cr_2O_3	0.05	0.04	0.05	0.04	0.07	0.04	0.02
T_{FeO}	24.84	23.71	23.59	22.72	20.82	19.63	21.46
MnO	1.29	1.44	0.41	0.37	0.40	0.48	0.39
MgO	4.02	6.00	7.94	8.14	8.33	6.39	6.50
CaO	0.01	0.03	0.06	–	0.03	0.06	0.00
Na_2O	0.10	0.14	0.12	0.11	0.11	0.11	0.11
K_2O	10.44	10.45	9.41	10.43	10.16	9.72	10.52
Total	94.25	95.68	95.83	96.15	92.40	91.59	97.11
O	24	24	24	24	24	24	24
Si	6.228	6.218	5.989	6.134	6.219	5.813	5.808
Ti	0.399	0.465	0.186	0.331	0.454	0.257	0.468
Al	3.105	2.867	3.469	3.066	2.803	4.219	3.788
Cr	0.007	0.005	0.007	0.005	0.010	0.004	0.003
Fe	3.646	3.409	3.336	3.214	3.041	2.859	2.971
Mn	0.192	0.209	0.059	0.053	0.059	0.079	0.055
Mg	1.052	1.538	2.000	2.052	2.178	1.643	1.605
Ca	0.002	0.005	0.011	–	0.006	0.014	0.001
Na	0.034	0.048	0.040	0.034	0.036	0.053	0.034
K	2.338	2.292	2.031	2.251	2.270	1.820	2.221
Total	17.003	17.051	17.191	17.201	17.074	16.755	16.952
Fe/(Fe + Mg)	0.78	0.69	0.63	0.61	0.58	0.62	0.65
T[§]	664	701	463	609	710	643	706

Note: [§]T represents estimated temperature by Ti-in-biotite thermometry according to Henry *et al.* (2005).

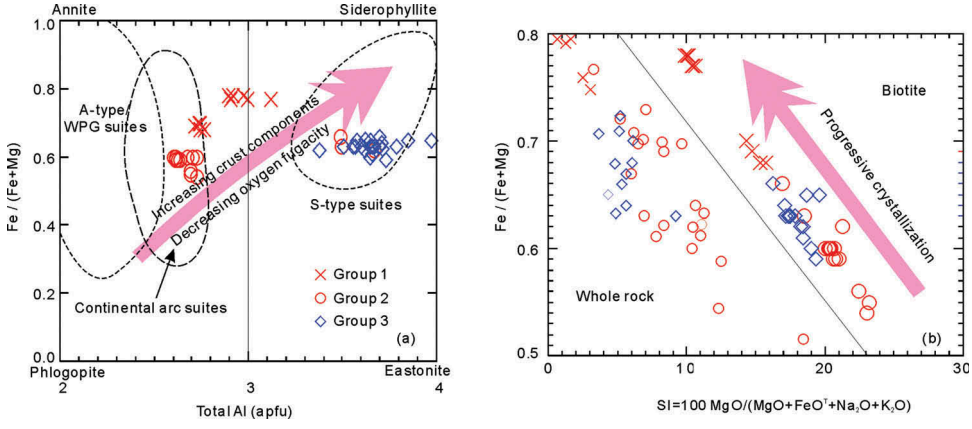

Figure 8. (a) Composition of biotite from the Weishan granites expressed in the Fe/(Fe + Mg) *versus* total Al diagram, also known as the annite-siderophyllite-phlogopite-eastonite quadrilateral (Shabani *et al*. 2003). (b) Fe/(Fe + Mg) *versus* the solidification index (SI) for biotite from the Weishan granites.

Table 6. Sr-Nd isotopic compositions of Weishan granites.

Sample	Age/ Ma	Rb(μg/ g)	Sr(μg/ g)	$^{87}Rb/^{86}Sr$	$^{87}Sr/^{86}Sr \pm 2s$	$(^{87}Sr/^{86}Sr)_i$	Sm(μg/ g)	Nd(μg/ g)	$^{147}Sm/^{144}Nd$	$^{143}Nd/^{144}Nd \pm 2s$	$e_{Nd}(t)$	T_{2DM} (Ma)*
HWS38	216	267.4	79.09	9.731	0.745048 ± 13	0.71516	7.498	36.45	0.1245	0.512048 ± 12	−9.5	1754
HWS40A	216	401.0	102.9	11.25	0.744592 ± 12	0.71003	5.953	28.78	0.1252	0.511958 ± 13	−11.3	1896
HWS42	222	241.8	106.3	6.542	0.735539 ± 14	0.71488	6.078	31.96	0.1151	0.512053 ± 14	−9.1	1746
HWS47	185	272.0	94.07	8.311	0.745633 ± 13	0.72377	3.600	19.64	0.1110	0.511928 ± 14	−11.8	1944

Note: * $t_{DM} = (1/l)\ln\{1 + [(^{143}Nd/^{144}Nd)_m - (^{143}Nd/^{144}Nd)_{DM} - ((^{147}Sm/^{144}Nd)_m - (^{147}Sm/^{144}Nd)_c)(e^t-1)]/[(^{147}Sm/^{144}Nd)_c - (^{147}Sm/^{144}Nd)_{DM}]\}$. T_{2DM} calculation is from Chen and Jahn (1998).

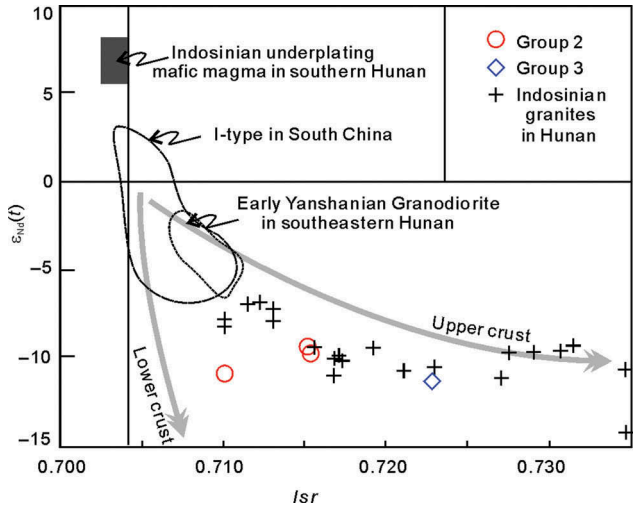

Figure 9. $\varepsilon_{Nd}(t)$ *versus* ISr diagram for the Weishan granites (Chen *et al*. 2007a). The data of Group 1 are from Wang *et al*. (2007) while those of Indosinian mafic magma and early Yanshanian granodiorite are from Guo *et al*. (1997), Zhao *et al*. (1998), Wang *et al*. (2003a), and Dai *et al*. (2008). The cross represents the Indosinian granitoids in other plutons of Hunan Province (Chen *et al*. 2006, 2007a; Wang *et al*. 2007).

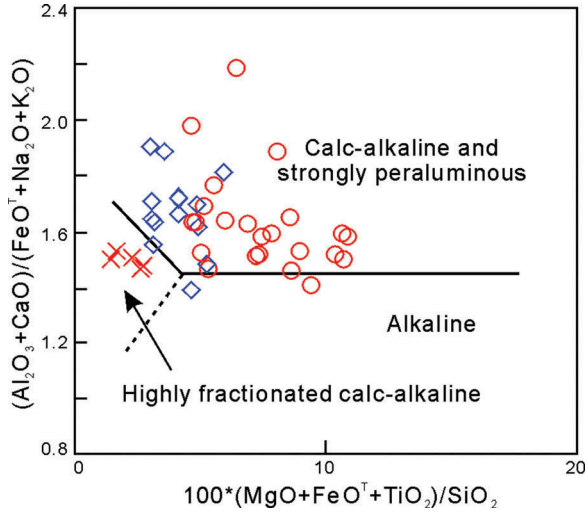

Figure 10. Classification diagram for the Weishan granites (Sylvester 1998). Symbols are as in Figure 8.

has been reported for highly fractionated granites from Northeastern China (Wu *et al*. 2003). Consequently, it is not unlikely that the precursor magma of the Xinpu biotite granite formed before 230 Ma. Moreover, a concordant age of 232 Ma and a cluster of older ages varying from 234 to 241 Ma found in the zircon cores from the W03 Xiangzikou tourmaline two-mica granite (Figure 4(f)) also reveals the occurrence of early-stage magmatism.

Therefore, we estimate that the Weishan granites were formed by episodic intrusion during the Middle to Late Triassic and again in Early Jurassic time. At least four stages of intrusion can be determined, i.e. 240–230 Ma, 220–215 Ma, 210–205 Ma, and ca. 185 Ma, with the 220–215 Ma stage being the main episode. Similar episodic magmatism also can be distinguished on the diagram of precise age frequency for the granitioids in Hunan and South China (Figure 11).

5.1.2. *Emplacement conditions*

Rough estimations of magma temperature for the Weishan granites were obtained by zircon saturation thermometry (Watson and Harrison 1983) and Ti-in-biotite thermometry (Henry *et al*. 2005). Zircon saturation thermometry presented a slightly elevated temperature trend, from Group 1 to Group 3 and Group 2 (Figure 12(a)). Low Zr concentrations (62.0–106.6 ppm) in Group 1 rocks yielded low estimated temperatures of 715–758°C, and Group 3 rocks were estimated at higher temperatures of 729–778°C because of their slightly high Zr concentrations (68.9–147.6 ppm). Group 2 rocks have the highest Zr concentrations, thus yielding the highest estimated temperatures of 786–831°C. Ti-in-biotite thermometry gave variable estimated temperature (Figure 12(b)), i.e. 652–715°C for Group 1, 303–719°C for Group 2, and 459–721°C for Group 3. The low estimated temperatures, coupled with low Ti concentrations, most likely indicate Ti losses or disequilibriums in biotites due to subsequent alteration (Henry *et al*. 2005), as some of biotite grains from the Weishan granites are partially chloritized with development of sagenitic rutile needles. Consequently, excluding temperatures <600°C, we obtain average temperatures of 679°C for Group 1, 708°C for Group 2, and 682°C for Group 3. Given that Ti-in-biotite thermometry reflects the

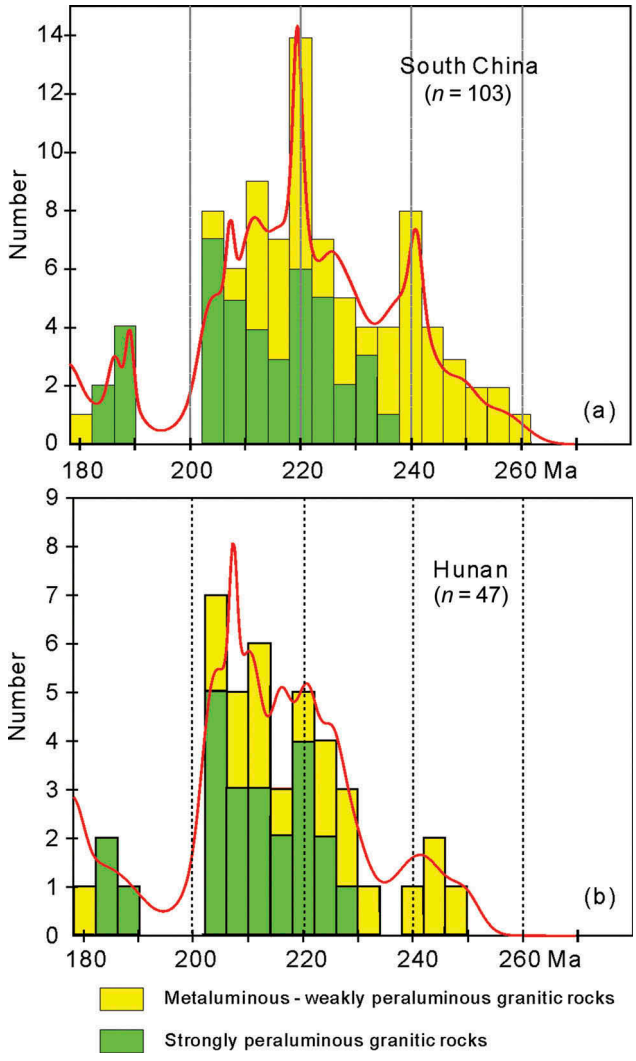

Figure 11. Age frequency of Triassic–Early Jurassic granitoids from South China (a) and Hunan Province (b) in terms of aluminous saturation index, showing the possible peak epoch of Triassic magmatism. The age data are from the references (Guo *et al*. 1997; Sun *et al*. 2002; Xu *et al*. 2003; Deng *et al*. 2004; Qiu *et al*. 2004; Zhang *et al*. 2004; Sun *et al*. 2005; Wang *et al*. 2005a; Chen *et al*. 2006; Ding *et al*. 2006; Peng *et al*. 2006; Chen *et al*. 2007a, 2007b, 2011; Wang *et al*. 2007; Dai *et al*. 2008; Fan *et al*. 2010; Liu *et al*. 2010; Sun *et al*. 2010; Cao *et al*. 2011; Han *et al*. 2011; Wang *et al*. 2012).

temperature of equilibrated magma with biotite (Henry *et al*. 2005), the average temperatures obtained by Ti-in-biotite thermometry are apparently lower than those by the zircon saturation thermometry. However, decrease in magma temperature from Group 2 to Group 3 and Group 1 is consistent with the trend revealed by the zircon saturation thermometry.

A qualitative evaluation of oxygen fugacity can be made from the Fe/(Fe + Mg) value of biotite by using the theoretical curve of Wones and Eugster (1965) in $f(O_2)$-T space for biotite + K-feldspar + magnetite equilibrium (Figure 13), which have been effectively applied to evaluate oxygen fugacity of orogenic granites (Lalonde and Bernard 1993; Shabani *et al*. 2003). On the basis of the temperatures calculated by the Ti-in-biotite thermometry, estimated $f(O_2)$ values range from 10^{-13} to 10^{-17} bars, displaying overall oxidizing conditions and an increasing trend in the order Group 1 < Group 3 < Group 2. Group 1 granitic melts mainly equilibrated at an oxygen fugacity between $10^{-15.5}$ and 10^{-17} bars, corresponding to conditions at the NNO buffer. Correspondingly, Group 2 granitic melts equilibrated at an oxygen fugacity between 10^{-13} and $10^{-14.5}$ bars, between the HM and NNO buffers, while Group 3 had an oxygen fugacity between $10^{-14.5}$ and $10^{-15.5}$ bars, above the NNO buffer. Lower oxygen fugacity for Group 1 granitic melts compared with other groups may be attributed to interfusion of a crust component during magma evolution (Figure 8(a)) and lower magma temperature. In despite of a changing trend in oxygen fugacity, the whole rocks show a trend of progressing Fe-enrichment in the order Group 2 > Group 3 > Group 1, with decreasing solidification indices that are mimicked by their biotite compositions (Figure 8(b)). This demonstrates that $f(O_2)$ was stable during progressive crystallization (Lalonde and Bernard 1993).

5.1.3. *Source nature*

Good correlations among major and trace elements for the whole rocks or among biotite chemical components suggest their affiliation in genesis for all the groups. As suggested by decreasing Al_2O_3, TiO_2, MgO, FeO^T, CaO, Sr, Zr, and La with increasing SiO_2 (Figure 6) and strongly negative Eu, Ba, Sr, P, and Ti anomalies (Figure 7), fractionation of K-feldspar, plagioclase, ilmenite and/or amphibole, biotite, and zircon is involved in magma evolution, where K-feldspar and plagioclase most likely play a crucial role (Figure 14). In the diagram of Sr *versus* Eu (Figure 15), all groups show almost the same slope trend. Because Eu is preferentially partitioned into K-feldspar and Sr into plagioclase during granitic magma evolution (Bea *et al*. 1994), the same slope trends for all the groups were thus produced by a similar fractionating assemblage in which the K-feldspar/plagioclase ratio is identical. As the different magma can hardly crystallize the same proportions of the same mineral assemblage under similar physical conditions, we suggest that those groups' granitic melts may be mainly derived from a single magma source. The significant trend of progressing Fe-enrichment with decreasing SI observed not only in the whole rocks but in the biotites from those three groups (Figure 8(b)) cannot be derived from a heterogeneous source. In addition, positive correlation of Ta *versus* SiO_2 also supports the viewpoint of a homogeneous source (Figure 6), because Ta is highly incompatible during magma differentiation and

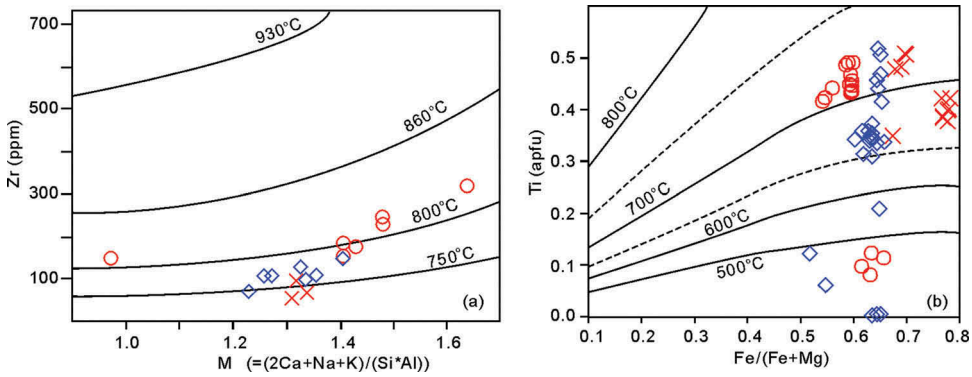

Figure 12. (a) Magma temperature estimated by zircon saturation thermometry (Watson and Harrison 1983) of the Weishan granites. (b) Magma temperature calculated by the thermometry of Ti-saturation in biotite (Henry *et al*. 2005) of the Weishan granites. Symbols are as in Figure 8.

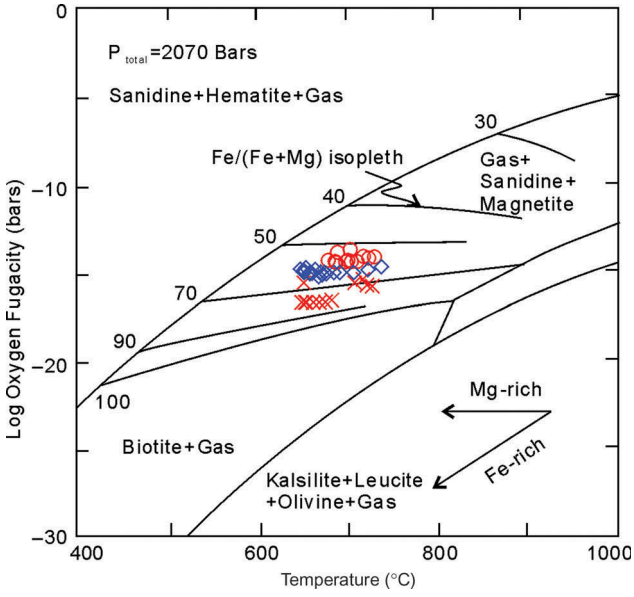

Figure 13. Log $f(O_2)$ – T diagram for the biotite + sanidine + magnetite + gas equilibrium at P_{total} = 2070 bars (Wones and Eugster 1965). The Weishan granites display elevated $f(O_2)$ from Group 1 to Group 3 and finally to Group 2. Symbols are as in Figure 8.

thus can be gradually enriched in the rocks (Green 1995; Ding *et al*. 2009).

Sr-Nd isotope and model age data suggest that the Weishan granites were derived by partial melting of Palaeoproterozoic crustal materials (Figure 9 and Table 6). On the source discrimination diagrams of Al_2O_3/TiO_2 *versus* CaO/Na_2O and (Na_2O + K_2O + FeO + MgO + TiO_2) *versus* (Na_2O + K_2O)/(FeO + MgO + TiO_2), both Group 2 and Group 3 rocks fall within the field of psammite (Figure 16(a)) and experimental melts derived by partial melting of metagreywackes (Figure 16(b)), while Group 1 rocks plot mainly in the field of pelite (Figure 16(a)) and experimental melts derived by partial melting of felsic pelites (Figure 16(b)). That seems to suggest that Group 1 rocks were derived from a different source than the other groups. However, given that the Al_2O_3/TiO_2 ratio is influenced by biotite and ilmenite fractionations and the CaO/Na_2O ratio by K-feldspar, plagioclase, and apatite fractionations (Sylvester 1998; Wang *et al*. 2007), Group 1, which is demonstrated as highly fractionated by feldspar (Figures 10 and 14), apatite, and Fe-rich oxides (Figure 6), need not be derived from a pelite source. Moreover, previous studies found that highly fractionated granite samples usually plot in

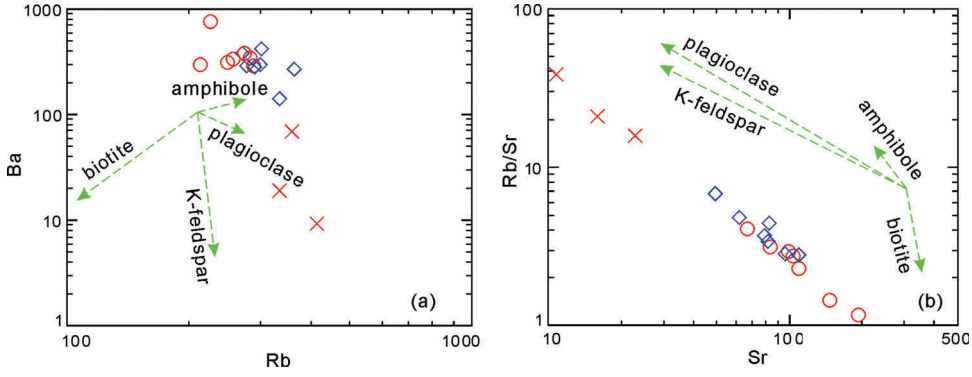

Figure 14. Diagrams of Ba *versus* Rb and Rb/Sr *versus* Sr, both of which indicate obvious crystal fractionation during the Weishan granitic magma evolution. Symbols are as in Figure 8.

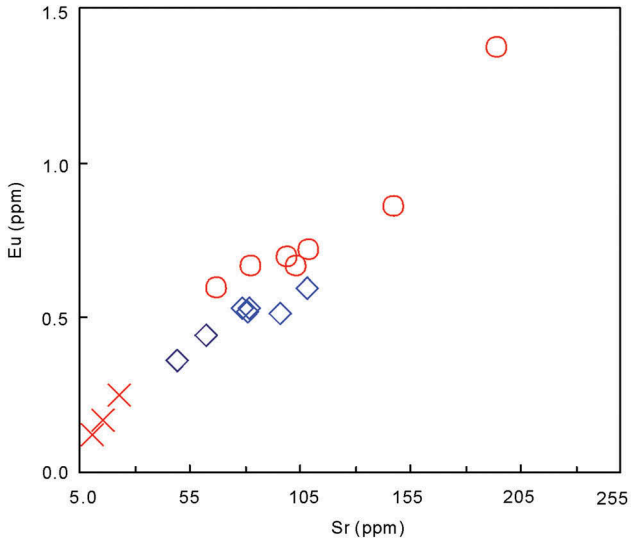

Figure 15. A diagram of Eu *versus* Sr. Almost the same slope trend for the groups implies that they formed by a very similar K-feldspar/plagioclase fractionating assemblage. Symbols are as in Figure 8.

the field of peraluminous leucogranites and experimental melts of felsic pelites on the source discrimination diagrams by Patiño Dounce (1999), even if they were generated by melting of a dominantly juvenile mantle component (Jahn *et al*. 2001). Therefore, we suggest that all the granite groups were derived by partial melting of Palaeoproterozoic psammitic crustal materials, such as metagreywackes and/or quartz amphibolites.

5.1.4. *Magmatic process*

Although all groups from the Weishan granite can be derived from a homogeneous source, their differences, less or more, in the composition and emplacement condition suggest that they might undergo diverse magmatic processes. First, dissimilar extents of crystal fractionation for those three groups result in different stages on the evolutionary trend, as mentioned above, where Group 2 and Group 1 rocks usually define two end-members of a trend, respectively. Second, there is no doubt that crustal contamination before or during magma emplacement was involved. For instance, in Figure 8(a) biotites from Group 1 and Group 3 samples show more siderophyllite end-members, implying increasing crustal components compared with those from Group 2 samples (Abdel-Rahman 1994; Shabani *et al*. 2003; Ding *et al*. 2012), consistent with the oxygen fugacity estimation. Furthermore, Group 3 rocks have higher initial $^{87}Sr/^{86}Sr$ (0.72377), close to the field of the upper crust in South China (Figure 9), also indicating component contamination from upper crust, as crustal contamination was generally observed in other Indosinian granites in South China (Chen *et al*. 2007a; Wang *et al*. 2007; Chen *et al*. 2011). Finally, partial melting of source materials also contributes to chemical differentiation in the Weishan granites. On the Sr *versus* Rb diagram, all three groups display more dispersive Sr concentrations than Rb (Figure 17(a)), indicating possible control by partial melting of source materials (Harris *et al*. 1995; Sylvester 1998; Wang *et al*. 2003a; Chen *et al*. 2007a). In contrast, Group 2 granitic melt was produced by greater partial melting of source materials. The obvious linear correlation between La and La/Yb ratios for the groups also suggests the importance of partial melting on the chemical differentiation of the Weishan granites (Figure 17(b)) (Wang *et al*. 2007). Note that Group 3 samples have higher slope trend and lower La concentrations than Group 2 examples on the La *versus* La/Yb diagram, suggesting that they might have originated by larger partial melting of source materials. The Weishan granites have high Rb concentrations (>200 ppm), which suggests a micaceous source. Previous studies found that muscovite dehydration melting can generally produce granite with high Rb/Sr (>5), with biotite dehydration melting causing low Rb/Sr (<5) granite (Harris *et al*. 1995; Visona and Lombardo 2002;

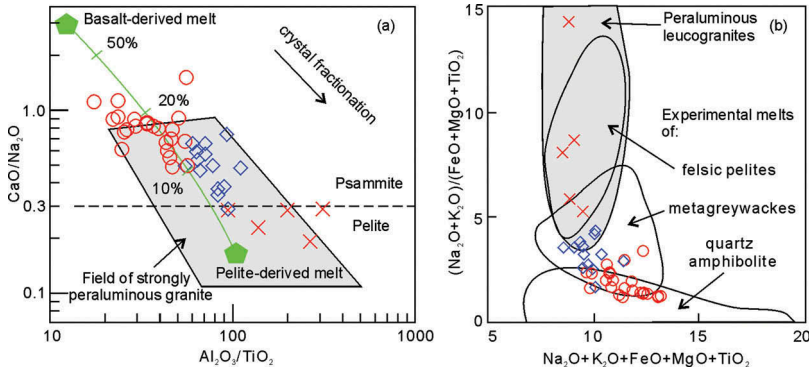

Figure 16. Diagrams of Al_2O_3/TiO_2 *versus* CaO/Na_2O (a) (Sylvester 1998), $Na_2O + K_2O + FeO + MgO + TiO_2$ *versus* $(Na_2O + K_2O)/(FeO + MgO + TiO_2)$ (b) (Patiño Dounce 1999) for the Weishan granites. Symbols are as in Figure 8.

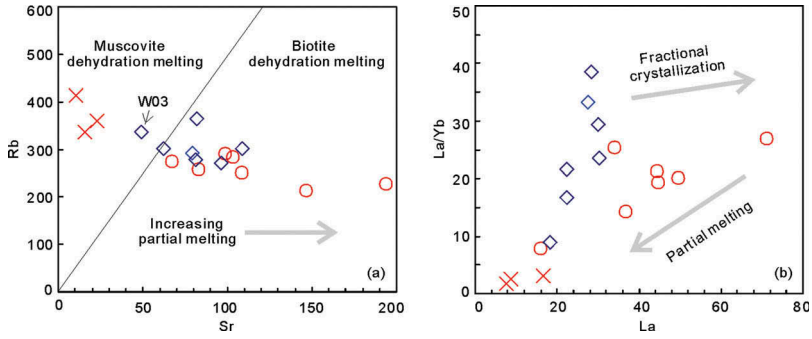

Figure 17. Diagrams of Rb *versus* Sr (a) and La *versus* La/Yb for the Weishan granites, displaying impact of partial melting on the chemical differentiation of the granites. Symbols are as in Figure 8.

Chen *et al*. 2007a; Wang *et al*. 2007). Most Weishan granites have low Rb/Sr ratios except Group 1 rocks and sample W03 (Figure 17(a)), suggesting that these granites were mainly derived by biotite dehydration melting during magma generation. Because Group 1 rocks experienced strong feldspar fractionation and thus have very low Sr concentrations (Figure 6(j)), we are not convinced that Group 1 is related to muscovite dehydration melting.

On the basis of the observations above, we propose a genetic model for the Weishan granites. In the Middle Triassic, low degree partial melting of Palaeoproterozoic psammitic materials produced a small magma chamber in the middle crust, which supplied magma to generate Group 1 Weishan granites. Later the magma chamber enlarged due to further partial melting of psammitic crustal materials involved in biotite dehydration, with temperature increasing in relation to tectonic events. The growing magma chamber supplied continuous heat to lower the cooling rate of Group 1 magma significantly, encouraging fractionation. On the other hand, it supplied a large volume of magma to produce the main body of Weishan granites, Group 2 rocks. During that time, the large magma chamber began chemical differentiation by exterior cooling and crystal fractionation (Petford *et al*. 2000; Burgisser and Bergantz 2011). Following this, another tectonic event supplied a new heat source, which reheated mushy magma in the lower part of the magma chamber, reducting its crystallinity. This process, called 'unzipping' by Burgisser and Bergantz (2011), can induce growth of a subjacent buoyant mobile magma layer with more aluminous (Burgisser and Bergantz 2011). When the magma layer became sufficiently buoyant and/or was activated by another new tectonic event, it could have penetrated the overlying mushy magma chamber and wrapped those previously formed zircons to the top, thus forming the Group 3 rocks in the Late Triassic. Probably due to continuous heating, this process can last for a long time and thus exported homogenized material from the lower mobile magma layer to the upper crust and continued until Early Jurassic time.

5.2. *Tectonic implications*

South China is the southeastern corner of the Eurasian continent, which has experienced interactions between the Eurasia, Pacific, Australia, and India plates and a variety of micro-plates in between. Therefore, it is important for deciphering the tectonic evolution of the present-day Eurasian plate. In the Mesozoic, continual plate interactions between the SCB and allochthonous continental blocks/oceanic plates initiated the formation of the eastern Eurasian plate (Metcalfe 2009). For example, along with closure of the Palaeo-Tethys Ocean, the ICB, the Simao Block, and the Qiangtang-Sibumasu Block were sequentially accreted to the SCB along the Ailaoshan–Red River suture in the Late Permian–Early Triassic (Metcalfe 1994; Lepvrier *et al*. 1997; Nam 1998; Carter *et al*. 2001; Nam *et al*. 2001; Lepvrier *et al*. 2004; Metcalfe 2009; Fan *et al*. 2010; Chen *et al*. 2011; Niu *et al*. 2011; Zhang *et al*. 2011), while the SCB was subducted northward beneath the North China Block (NCB) to form the Qinling–Dabie orogen (Li *et al*. 1993; Zhang 1997; Hacker *et al*. 1998; Meng and Zhang 2000; Sun *et al*. 2002; Liu *et al*. 2006; Li *et al*. 2010), consequently shaping the Songpan–Garze fold belt separated by the Longmenshan thrust-nappe belt from the SCB (Chen and Wilson 1996; Huang *et al*. 2003; Roger *et al*. 2004; Harrowfield and Wilson 2005; Hu *et al*. 2005) (Figure 1(a)). These continental blocks were finally welded together, followed by the subduction of Palaeo-Pacific plate beneath the newly formed eastern Eurasian plate either in Permo-Triassic time (Wang *et al*. 2005a; Li and Li 2007) or in the Jurassic (Jahn *et al*. 1976; Maruyama *et al*. 1997; Zhou and Li 2000; Zhou *et al*. 2006; Sun *et al*. 2007; Wang *et al*. 2011; Li *et al*. 2012; Sun *et al*. 2012). Correspondingly, great volumes of Mesozoic granitoid-volcanic rocks, mineral deposits, and a series of thrusts and ductile shear zones formed throughout an area roughly 1300 km wide and 2000 km long, from the coastal areas to the SCB interior (Chen 1999; Zhou and Li 2000; Hua *et al*. 2003; Li *et al*. 2003; Yan *et al*. 2003; Zhou *et al*. 2006; Li and Li 2007; Shu *et al*. 2008; Shu *et al*. 2009; Wang *et al*. 2011; Sun *et al*. 2012;

Wang *et al*. 2012). Thus the SCB has experienced a complex magmatic and tectonic history due to the interactions of four major plates, namely the SCB, the NCB, the ICB, and the Palaeo-Pacific plate.

Four major hypotheses on the genesis of Indosinian granitoids in South China have been proposed: (1) partial melting of thickened crust related to the ICB–SCB collision (Sun *et al*. 2005; Ding *et al*. 2006; Zhou *et al*. 2006; Chen *et al*. 2007a; Wang *et al*. 2007); (2) intra-continental collision (e.g. Yangtze–Cathaysian collision) within the SCB (Wang *et al*. 2003b, 2005b); (3) derivation from newly underplated magma in response to upwelling asthenosphere (Guo *et al*. 1997; Zhao *et al*. 1998; Wang *et al*. 2001); and (4) subduction of an oceanic plate (Hsü *et al*. 1990; Gilder *et al*. 1996; Wang *et al*. 2005a; Li *et al*. 2006). However, the Weishan granites were formed during a long period from the Middle Triassic to the Early Jurassic. Individual tectonic events cannot explain their genesis.

In the FeO^T-MgO-Al_2O_3 diagram of Abdel-Rahman (1994), biotites from Group 2 rocks plot between the calc-alkaline and peraluminous fields, whereas biotites from other groups fall in the peraluminous field (Figure 18(a)). This implies that generation of Group 2 rocks was related to orogenic events, and that other groups were related to some collision processes (Abdel-Rahman 1994; Shabani *et al*. 2003). In the Hf-Rb/30-3*Ta diagram of Harris *et al*. (1986), Group 2 rocks plot in the late or post-collision field, whereas other groups fall in the syn-collision field (Figure 18(b)).

It is well known that Indosinian movement was related to continental collision between the ICB and SCB, with the startup at ca. 267–262 Ma (Li *et al*. 2006) and the peak metamorphism at ca. 258–243 Ma in the collision zone (Lepvrier *et al*. 1997; Nam 1998; Carter *et al*. 2001; Maluski *et al*. 2001; Nam *et al*. 2001; Lepvrier *et al*. 2004; Chen *et al*. 2011). However, the peak metamorphism of Indosinian events in South China occurred at ca. 230 Ma (Wang *et al*. 2012) and Qingling-Dabie occurred during 230–226 Ma (Chen *et al*. 2007a), indicating that the stress from Indosinian movement gradually increased from south to north (Ding *et al*. 2006). Therefore, Group 1 rocks from the Weishan granites, formed during 240–230 Ma, were probably produced by partial melting of thickened crustal components during prograde metamorphism due to the collision of the ICB and SCB. Because of the compressive stress, granitic magmatism is really constrained (Sylvester 1998).

Experimental and theoretical studies have demonstrated that compressive stress and heat can usually be released at ~5–20 million years following peak stacking of the thickened crust (Patiño Dounce, Humphreys, and Johnson 1990; Wang *et al*. 2007). Stress and heat relaxation will favour crustal extension and partial melting by decompression to generate a large volume of peraluminous granitic magma (Sylvester 1998). This can reasonably explain why the Indosinian granites in South China were mainly produced during ca. 220–215 Ma (Figures 11 and 19), as was the main body, Group 2 of the Weishan granites. Previous studies have proved that 233–220 Ma mafic magma underplating in the lower continental crust might have ocurred in Hunan Province (Figure 19) (Guo *et al*. 1997; Jiang *et al*. 2009; Liu *et al*. 2012). The underplated mafic magma most likely furthered partial melting of crust and generation of granitic magma. More importantly, it probably supplied additional heat to the cooling magma chamber, so as to rapidly remobilize initially mushy magma in the lower part of the magma chamber into a peraluminous magma layer, as proposed by our model. When the magma layer became more and more buoyant, it penetrated the overlying mushy magma chamber to generate peraluminous granites, just like Group 3 of the Weishan granites. Before that, the SCB was rapidly uplifted toward the surface following its deep subduction beneath the NCB (Li *et al*. 1993; Hacker *et al*. 1998; Li *et al*. 2010). This event probably resulted in regional compression, heating, and intracontinental collision, especially in a weak zone between the Yangtze and the

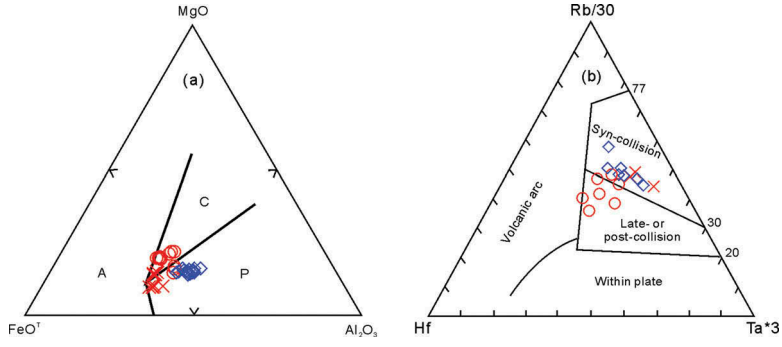

Figure 18. (a) Composition of biotite from the Weishan granites expressed in the discrimination diagrams of Abdel-Rahman (1994). A, anorogenic extension-related peralkaline granites; C, subduction-related calc-alkaline orogenic suites; P, peraluminous granites in a collision setting. (b) Tectonic discrimination diagram of Harris *et al*. (1986) on the Weishan granites. Symbols are as in Figure 8.

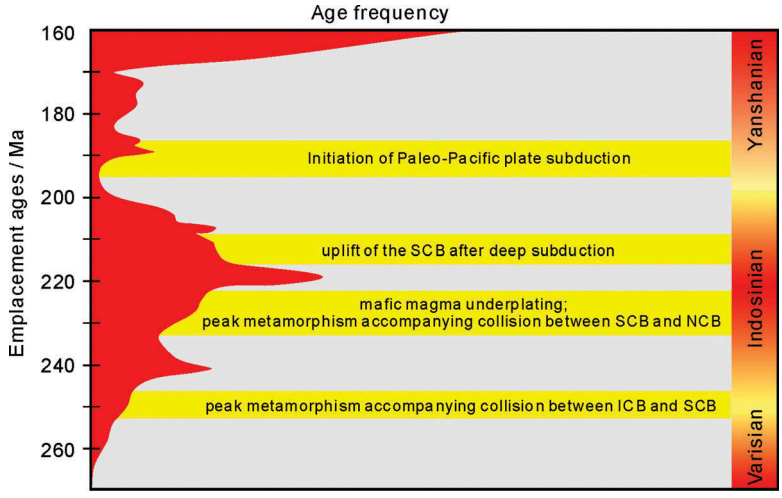

Figure 19. Age summary diagram between the frequency of ages for the Indosinian–early Yanshanian granites in the SCB and major tectonothermal events. Ages for the Indosinian–early Yanshanian granites in the SCB are as in Figure 11.

Cathaysian blocks (Wang *et al*. 2003b, 2005b), such as the Xuefengshan tectonic belt. The Weishan granites located among the Jiangshan–Shaoxing, Jingxian–Anhua, and Chenxian–Linwu faults (Figure 1) have been considered as products of the Indosinian intracontinental collision (Wang *et al*. 2005b) and early Yanshanian crustal detachment collision (Wang *et al*. 2003b). In regard to the Early Jurassic magmatism, it was probably controlled by the crustal detachment collision between the Yangtze and Cathaysia blocks (Wang *et al*. 2003b), probably associated with the subduction of the Palaeo-Pacific oceanic plate beneath the Eurasia plate (Figure 19).

In general, the Weishan granites were generated by multiple magma processes, in response to continuous tectonothermal events during Middle Triassic to Early Jurassic times, irrespective of tectonic settings. Continuous tectonic activities can promote not only partial melting of source materials, but also control magma evolution, and can finally make space in the crust for magma ascent and emplacement.

6. Conclusion

This paper studied a representative composite granitic intrusion in South China, the Weishan granites, which can be divided into three groups in terms of geochemistry, mineralogy, and geochronology. The results are as follows:

(1) Bulk and biotite compositions from all the groups define a good linear trend, with Group 1 and Group 2 samples defining two mixing end-members. Group 1 rocks are highly fractionated, weakly peralumious (ACNK = 1.0–1.1), and have extremely low solidification indices (1.0–3.0), with flatter REE patterns ((La/Yb)N = 1.1–2.0), lower ΣLREE/ΣHREE ratios (1.5–2.4), and more negative Eu, Ba, Sr, P, and Ti anomalies compared with other groups. Group 2 rocks show metaluminous-peralumious (0.9–1.5), with higher MgO and FeO, slightly higher $\varepsilon_{Nd}(t)$, and lower initial $^{87}Sr/^{86}Sr$ than those of Group 3. Group 3 rocks show overall strong peraluminous, with moderately low SI (2.3–9.3) and moderately high values of ACNK (1.05–1.20), SiO_2, and Al_2O_3. Studies on zircon saturation thermometry, Ti-in-biotite thermometry, and an evaluation of biotite oxygen fugacity indicated that precursor magmas of the three groups were emplaced at overall oxidizing conditions at relatively low temperature (<830°C). Geochemical studies suggest that the precursor magmas were mainly derived by partial melting of Palaeoproterozoic psammites but were subsequently differentiated by fractional crystalization, crustal contamination, and partial melting.

(2) Single mica Rb-Sr isochron dating for the Weishan granites yields three ages, 227.0 ± 13 Ma for biotites in Group 1 rocks, 221.9 ± 5.8 Ma for biotites in Group 2 rocks, and 210.1 ± 3.3 Ma for muscovites in Group 3 rocks. LA-ICP-MS zircon U-Pb dating results indicate that Group 2 rocks were formed at 215.7 ± 1.9 Ma, while Group 3 rocks were generated during two episodes of 211.0 ± 1.6 Ma ~ 207.9 ± 1.9 Ma and 187.4 ± 3.5 Ma ~ 184.5 ± 5.1 Ma. Meanwhile, LA-ICP-MS zircon U-Pb dating for Group 3 rocks obtained zircon core ages of 232–237 Ma, 221.5 ± 0.8 Ma, and 219.8 ± 1.6 Ma. Therefore, we propose that Weishan granites were generated during at least four stages of intrusion, i.e. 240–

230 Ma for Group 1, 220–215 Ma for Group 2, 210–205 Ma, and ca. 185 Ma for Group 3, with the stage of 220–215 Ma being the main episode.

(3) The Weishan granites were generated by multiple magma processes, in response to continuous tectonothermal events during the Middle Triassic to Early Jurassic time, irrespective of tectonic settings. We propose that the oldest Group 1 granitic melts were derived by low-degree partial melting of thickened Palaeoproterozoic psammitic crustal materials during prograde metamorphism due to the collision of the ICB and SCB. The younger (Group 2) melts were generated by further partial melting of psammitic crustal materials in response to stress relaxation in the post-collision stage and regional conductive heating from underplating mafic magma. The youngest (Group 3) magmas represent remobilized buoyant magma pulses from a mushy Group 2 magma source accompanying regional heating, probably resulting from the Indosinian intracontinental deformation and the early Yanshanian crustal detachment collision, which might be associated with the uplift of the SCB following its deep subduction along the Dabie orogeny and the subduction of the palaeo-Pacific oceanic plate beneath the Eurasia plate, respectively.

Acknowledgements

The authors thank Prof. X. Zhou for discussions and F. Wang and L. Chen for help with the sample EPMA analyses. Prof. Robert E. Zartman polished the manuscript and improved the English. Reviews by two anonymous referees and the comments of Prof. Robert Stern have greatly helped improve the paper. This is also a contribution by No. IS-1860 from GIGCAS.

Funding

This study was supported jointly by the Ministry of Science and Technology of China [2012CB416703]; the National Natural Science Foundation of China [41090373], [41372005], and [41121002]; the State Key Laboratory of Isotope Geochemistry, Guangzhou Institute of Geochemistry, CAS [GIGIso-QD-12-04, Y436021A07DX]; and the 135 project of GIGCAS [Y234152001].

References

Abdel-Rahman, A.M., 1994, Nature of biotites from alkaline, calc-alkaline, and peraluminous magmas: Journal of Petrology, v. 35, p. 525–541. doi:10.1093/petrology/35.2.525

Bea, F., Pereira, M.D., and Stroh, A., 1994, Mineral/leucosome trace-element partitioning in a peraluminous migmatite (a laser ablation-ICP-MS study): Chemical Geology, v. 117, p. 291–312. doi:10.1016/0009-2541(94)90133-3

Burgisser, A., and Bergantz, G.W., 2011, A rapid mechanism to remobilize and homogenize highly crystalline magma bodies: Nature, v. 471, p. 212–215. doi:10.1038/nature09799

Cao, S.H., Tang, F.L., Huang, X.S., Qiu, W.J., and Yuan, Z.G., 2011, Characteristics and zircon U-Pb geochronology of metallogenic granitoids in the Gaojiashan Cu-Mo deposits, Northern Wuyishan, Jiangxi Province: Acta Geologica Sinica, v. 85, no. 2, p. 207–212.

Carter, A., Roques, D., Bristow, C., and Kinny, P., 2001, Understanding Mesozoic accretion in Southeast Asia: Significance of Triassic thermotectonism (Indosinian orogeny) in Vietnam: Geology, v. 29, no. 3, p. 211–214. doi:10.1130/0091-7613(2001)029<0211:UMAISA>2.0.CO;2

Chappell, B.W., 1999, Aluminium saturation in I- and S-type granites and the characterization of fractionated haplogranites: Lithos, v. 46, p. 535–551. doi:10.1016/S0024-4937(98)00086-3

Chen, A., 1999, Mirror-image thrusting in the South China Orogenic Belt: Tectonic evidence from western Fujian, southeastern China: Tectonophysics, v. 305, p. 497–519. doi:10.1016/S0040-1951(99)00036-0

Chen, C.H., Hsieh, P.S., Lee, C.Y., and Zhou, H.W., 2011, Two episodes of the Indosinian thermal event on the South China Block: Constraints from LA-ICPMS U-Pb zircon and electron microprobe monazite ages of the Darongshan S-type granitic suite: Gondwana Research, v. 19, no. 4, p. 1008–1023. doi:10.1016/j.gr.2010.10.009

Chen, J.F., and Jahn, B.M., 1998, Crustal evolution of southeastern China: Nd and Sr isotopic evidence: Tectonophysics, v. 284, p. 101–133. doi:10.1016/S0040-1951(97)00186-8

Chen, S.F., and Wilson, C.J.L., 1996, Emplacement of the Longmen Shan Thrust-Nappe Belt along the eastern margin of the Tibetan Plateau: Journal of Structural Geology, v. 18, p. 413–430. doi:10.1016/0191-8141(95)00096-V

Chen, W.F., Chen, P.R., Huang, H.Y., Ding, X., and Sun, T., 2007a, Chronological and geochemical studies of granite and enclave in Baimashan pluton, Hunan, South China: Science in China Series D: Earth Sciences, v. 50, no. 11, p. 1606–1627. doi:10.1007/s11430-007-0073-1

Chen, W.F., Chen, P.R., Zhou, X.M., Huang, H.Y., Ding, X., and Sun, T., 2006, Single zircon LA-ICP-MS U-Pb dating of the Yangmingshan granitic pluton in Hunan, South China and its petrogenetic study: Acta Geologica Sinica, v. 80, no. 7, p. 1065–1077.

Chen, W.F., Chen, P.R., Zhou, X.M., Huang, H.Y., Ding, X., and Sun, T., 2007b, Single zircon LA-ICP-MS U-Pb dating of the Guandimiao and Wawutang granitic plutons in Hunan, South China and its petrogenetic significance: Acta Geologica Sinica, v. 81, no. 1, p. 801–840.

Dai, B.Z., Jiang, S.Y., Jiang, Y.H., Zhao, K.D., and Liu, D.Y., 2008, Geochronology, geochemistry and Hf-Sr-Nd isotopic compositions of Huziyan mafic xenoliths, southern Hunan Province, South China: Petrogenesis and implications for lower crust evolution: Lithos, v. 102, no. 1–2, p. 65–87. doi:10.1016/j.lithos.2007.08.010

Deng, X.G., Chen, Z.G., Li, X.H., and Liu, D.Y., 2004, SHRIMP U-Pb zircon dating of the Darongshan-Shiwandashan granitoid belt in southeastern Guangxi, China: Geological Review, v. 50, no. 4, p. 426–432.

Ding, X., Sun, W.D., Wang, F.Y., Chen, L.L., Li, Q.L., and Chen, F.K., 2012, Single-grain mica Rb-Sr isochron ages and mineral chemistry for the Weishan pluton in Hunan province and implications on petrogenesis and mineralization of Mesozoic composite granite in South China: Acta Petrologica Sinica, v. 28, no. 12, p. 3823–3840.

Ding, X., Chen, P.R., Chen, W.F., Huang, H.Y., and Zhou, X.M., 2006, Single zircon LA-ICPMS U-Pb dating of Weishan granite (Hunan, South China) and its petrogenetic significance: Science in China Series D: Earth Sciences, v. 49, no. 8, p. 816–827. doi:10.1007/s11430-006-0816-4

Ding, X., Lundstrom, C., Huang, F., Li, J., Zhang, Z., Sun, X., Liang, J., and Sun, W., 2009, Natural and experimental constraints on formation of the continental crust based on niobium-tantalum fractionation: International Geology Review, v. 51, no. 6, p. 473–501. doi:10.1080/00206810902759749

Fan, W., Wang, Y., Zhang, A., Zhang, F., and Zhang, Y., 2010, Permian arc-back-arc basin development along the Ailaoshan tectonic zone: Geochemical, isotopic and geochronological evidence from the Mojiang volcanic rocks, Southwest China: Lithos, v. 119, p. 553–568. doi:10.1016/j.lithos.2010.08.010

Gilder, S.A., Gill, J., Coe, R.S., Zhao, X., Liu, Z., Wang, G., Yuan, K., Liu, W., Kuang, G., and Wu, H., 1996, Isotopic and paleomagnetic constraints on the Mesozoic tectonic evolution of south China: Journal of Geophysical Research-Solid Earth, v. 101, no. B7, p. 16137–16154. doi:10.1029/96JB00662

Green, T.H., 1995, Significance of Nb/Ta as an indicator of geochemical processes in the Crust-Mantle System: Chemical Geology, v. 120, no. 3–4, p. 347–359. doi:10.1016/0009-2541(94)00145-X

Guo, F., Fan, W.M., Lin, G., and Lin, Y.X., 1997, Sm-Nd isotopic age and genesis of gabbro xenoliths in Daoxian County, Hunan Province: Chinese Science Bulletin, v. 42, no. 21, p. 1814–1817. doi:10.1007/BF02882650

Hacker, B.R., Ratschbacher, L., Webb, L., Ireland, T., Walker, D., and Shuwen, D., 1998, U/Pb zircon ages constrain the architecture of the ultrahigh-pressure Qinling–Dabie Orogen, China: Earth and Planetary Science Letters, v. 161, p. 215–230. doi:10.1016/S0012-821X(98)00152-6

Han, J., Wang, Y.B., Wang, D.H., Chen, Z.H., and Hou, K.J., 2011, Age and genesis of the granite in the Huangfengling uranium deposit, Jiangxi Province: Evidence from zircon U-Pb dating and Hf isotopes: Geology and Exploration, v. 47, no. 2, p. 284–293.

Harris, N., Ayres, M., and Massey, J., 1995, Geochemistry of granitic melts produced during the incongruent melting of muscovite: Implications for the extraction of Himalayan leucogranite magmas: Journal of Geophysical Research, v. 100, p. 15767–15777. doi:10.1029/94JB02623

Harris, N.B.W., Pearce, J.A., and Tindle, A.G., 1986, Geochemical characteristics of collision-zone magmatism, *in* Coward, M.P., and Reis, A.C., eds., Collision tectonics: Geological Society of London, Special Publications, v. 19, p. 67–81.

Harrowfield, M.J., and Wilson, C.J.L., 2005, Indosinian deformation of the Songpan Garzê Fold Belt, northeast Tibetan Plateau: Journal of Structural Geology, v. 27, p. 101–117. doi:10.1016/j.jsg.2004.06.010

Henry, D.J., Guidotti, C.V., and Thomson, J.A., 2005, The Ti-saturation surface for low-to-medium pressure metapelitic biotites: Implications for geothermometry and Ti-substitution mechanisms: American Mineralogist, v. 90, p. 316–328. doi:10.2138/am.2005.1498

HNGBMR (Bureau of Geology and Mineral Resources of Hunan Province), 1988, Regional geology of Hunan province: Beijing, Grological Publishing House, p. 1–507.

Hsü, K.J., Li, J., Chen, H., Wang, Q., Sun, S., and Şengör, A.M.C., 1990, Tectonics of South China: Key to understanding West Pacific geology: Tectonophysics, v. 183, no. 1–4, p. 9–39. doi:10.1016/0040-1951(90)90186-C

Hu, J.M., Meng, Q.R., Shi, Y.R., and Qu, H.J., 2005, SHRIMP U-Pb dating of zircons from granitoid bodies in the Songpan-Ganzi terrane and its implications: Acta Petrologica Sinica, v. 21, no. 3, p. 867–880.

Hua, R.M., Chen, P., Zhang, W., Liu, X., Lu, J., Lin, J., Yao, J., Qi, H., Zhang, Z., and Gu, S., 2003, Metallogenic systems related to Mesozoic and Cenozoic granitoids in South China: Science in China Series D: Earth Sciences, v. 46, no. 8, p. 816–829. doi:10.1007/BF02879525

Huang, M., Maas, R., Buick, I.S., and Williams, I.S., 2003, Crustal response to continental collisions between the Tibet, Indian, South China and North China Blocks: Geochronological constraints from the Songpan-Garzê Orogenic Belt, western China: Journal of Metamorphic Geology, v. 21, no. 3, p. 223–240. doi:10.1046/j.1525-1314.2003.00438.x

Huang, X., and Wu, L.R., 1990, Nd-Sr isotopes of granitoids from Shanxi Province and their significance for tectonic evolution: Acta Petrologica Sinica, v. 6, no. 2, p. 1–11.

Jahn, B.M., Chen, P.Y., and Yen, T.P., 1976, Rb-Sr ages of granitic rocks in southeastern China and their tectonic significance: Geological Society of America Bulletin, v. 87, p. 763–776. doi:10.1130/0016-7606(1976)87<763:RAOGRI>2.0.CO;2

Jahn, B.M., Wu, F., Capdevila, R., Martineau, F., Zhao, Z., and Wang, Y., 2001, Highly evolved juvenile granites with tetrad REE patterns: The Woduhe and Baerzhe granites from the Great Xing'an Mountains in NE China: Lithos, v. 59, p. 171–198. doi:10.1016/S0024-4937(01)00066-4

Jenkin, G.R.T., Ellam, R.M., Rogers, G., and Stuart, F.M., 2001, An investigation of closure temperature of the biotite Rb-Sr system: The importance of cation exchange: Geochimica Et Cosmochimica Acta, v. 65, no. 7, p. 1141–1160. doi:10.1016/S0016-7037(00)00560-3

Jiang, Y.H., Jiang, S., Dai, B., Liao, S., Zhao, K., and Ling, H., 2009, Middle to Late Jurassic felsic and mafic magmatism in southern Hunan province, southeast China: Implications for a continental arc to rifting: Lithos, v. 107, no. 3–4, p. 185–204. doi:10.1016/j.lithos.2008.10.006

Lalonde, A.E., and Bernard, P., 1993, Composition and Color of Biotite from Granites – 2 Useful Properties in the Characterization of Plutonic Suites from the Hepburn Internal Zone of Wopmay Orogen, Northwest-Territories: Canadian Mineralogist, v. 31, p. 203–217.

Lepvrier, C., Maluski, H., Van Tich, V.U., Leyreloup, A., Truong Thi, P., and Van Vuong, N., 2004, The Early Triassic Indosinian orogeny in Vietnam (Truong Son Belt and Kontum Massif); implications for the geodynamic evolution of Indochina: Tectonophysics, v. 393, no. 1–4, p. 87–118. doi:10.1016/j.tecto.2004.07.030

Lepvrier, C., Maluski, H., Van Vuong, N., Roques, D., Axente, V., and Rangin, C., 1997, Indosinian NW-trending shear zones within the Truong Son belt (Vietnam) ^{40}Ar-^{39}Ar Triassic ages and Cretaceous to Cenozoic overprints: Tectonophysics, v. 283, no. 1–4, p. 105–127. doi:10.1016/S0040-1951(97)00151-0

Li, C.Y., Zhang, H., Wang, F., Liu, J., Sun, Y., Hao, X., Li, Y., and Sun, W., 2012, The formation of the Dabaoshan porphyry molybdenum deposit induced by slab rollback: Lithos, v. 150, p. 101–110. doi:10.1016/j.lithos.2012.04.001

Li, Q., Chen, F., Wang, X., Li, X., and Li, C., 2005, Ultra-low procedural blank and the single-grain mica Rb-Sr isochron dating: Chinese Science Bulletin, v. 50, no. 24, p. 2861–2865.

Li, S., Xiao, Y., Liou, D., Chen, Y., Ge, N., Zhang, Z., Sun, S., Cong, B., Zhang, R., and Hart, S.R., 1993, Collision of the North China

and Yangtse Blocks and formation of coesite-bearing eclogites: Timing and processes: Chemical Geology, v. 109, no. 1–4, p. 89–111. doi:10.1016/0009-2541(93)90063-O

Li, S.Z., Kusky, T.M., Zhao, G., Liu, X., Zhang, G., Kopp, H., and Wang, L.U., 2010, Two-stage Triassic exhumation of HP-UHP terranes in the western Dabie orogen of China: Constraints from structural geology: Tectonophysics, v. 490, no. 3–4, p. 267–293. doi:10.1016/j.tecto.2010.05.010

Li, X.H., Chen, Z.G., Liu, D.Y., and Li, W.X., 2003, Jurassic gabbro-granite-syenite suites from southern Jiangxi Province, SE China: Age, origin, and Tectonic significance: Lithos, v. 45, no. 10, p. 898–921.

Li, X.H., Li, Z.X., Li, W.X., and Wang, Y.J., 2006, Initiation of the Indosinian Orogeny in South China: Evidence for a Permian magmatic arc on Hainan Island: The Journal of Geology, v. 114, no. 3, p. 341–353. doi:10.1086/501222

Li, Z.X., and Li, X.H., 2007, Formation of the 1300-km-wide intracontinental orogen and postorogenic magmatic province in Mesozoic South China: A flat-slab subduction model: Grology, v. 35, no. 3, p. 179–182.

Liang, J.L., Ding, X., Sun, X.M., Zhang, Z.M., Zhang, H., and Sun, W.D., 2009, Nb/Ta fractionation observed in eclogites from the Chinese Continental Scientific Drilling Project: Chemical Geology, v. 268, p. 27–40. doi:10.1016/j.chemgeo.2009.07.006

Liang, Q., Hu, J., and Gregoire, D.C., 2000, Determination of trace elements in granites by inductively coupled plasma mass spectrometry: Talanta, v. 51, p. 507–513. doi:10.1016/S0039-9140(99)00318-5

Liu, C.-Z., Liu, Z.-C., Wu, F.-Y., and Chu, Z.-Y., 2012, Mesozoic accretion of juvenile sub-continental lithospheric mantle beneath South China and its implications: Geochemical and Re-Os isotopic results from Ningyuan mantle xenoliths: Chemical Geology, v. 291, p. 186–198. doi:10.1016/j.chemgeo.2011.10.006

Liu, F.L., Gerdes, A., Liou, J.G., Xue, H.M., and Liang, F.H., 2006, SHRIMP U-Pb zircon dating from Sulu-Dabie dolomitic marble, eastern China: Constraints on prograde, ultra-high-pressure and retrograde metamorphic ages: Journal of Metamorphic Geology, v. 24, no. 7, p. 569–589. doi:10.1111/j.1525-1314.2006.00655.x

Liu, Y., Li, T.D., Xiao, Q.H., Geng, S.F., Wang, T., and Chen, B. H., 2010, New chronology of the Ningyuan alkali basalt in southern Hunan, China: Evidence from LA-ICP-MS zircon U-Pb dating: Geological Bulletin of China, v. 29, no. 6, p. 833–841.

Liu, Y.S., Hu, Z., Gao, S., Gunther, D., Xu, J., Gao, C., and Chen, H., 2008, In situ analysis of major and trace elements of anhydrous minerals by LA-ICP-MS without applying an internal standard: Chemical Geology, v. 257, no. 1–2, p. 34–43. doi:10.1016/j.chemgeo.2008.08.004

Ludwig, K.R., 1991, ISOPLOT: A plotting and regression program for radiogenic-isotope data. US Geological Survey Open-File Report, 39 p.

Maluski, H., Lepvrier C, Jolivet L, Carter A, Roques D, Beyssac O, Tang T.T., Thang N.D., and Avigad, D., 2001, Ar-Ar and fission-track ages in the Song Chay Massif: Early Triassic and Cenozoic tectonics in northern Vietnam: Journal of Asian Earth Sciences, v. 19, no. 1–2, p. 233–248. doi:10.1016/S1367-9120(00)00038-9

Maruyama, S., Isozaki, Y., Kimura, G., and Terabayashi, M., 1997, Paleogeographic maps of the Japanese Islands: Plate tectonic synthesis from 750 Ma to the present: The Island Arc, v. 6, no. 1, p. 121–142. doi:10.1111/j.1440-1738.1997.tb00043.x

Meng, Q.R., and Zhang, G.W., 2000, Geologic framework and tectonic evolution of the Qinling orogen, central China: Tectonophysics, v. 323, p. 183–196. doi:10.1016/S0040-1951(00)00106-2

Metcalfe, I., 1994, Gondwanaland origin, dispersion, and accretion of East and Southeast Asian continental terranes: Journal of South American Earth Sciences, v. 7, no. 3–4, p. 333–347. doi:10.1016/0895-9811(94)90019-1

Metcalfe, I., 2009, Late Palaeozoic and Mesozoic tectonic and palaeogeographical evolution of SE Asia, *in* Buffetaut, E., Cuny, G., Le Loeuff, J., and Suteethorn, V., eds., Late Palaeozoic and Mesozoic ecosystems in SE Asia: The Geological Society of London, Special Publications, v. 315, p. 7–23.

Nam, T.N., 1998, Thermotectonic events from Eparly Proterozoic to Miocene in the Indochina craton: Implication of K–Ar ages in Vietnam. Journal of Asian Earth Sciences, v. 16, no. 5–6, p. 475–484. doi:10.1016/S0743-9547(98)00027-0

Nam, T.N., Sano, Y., Terada, K., Toriumi, M., Van Quynh, P., and Dung, L.T., 2001, First SHRIMP U-Pb zircon dating of granulites from the Kontum massif (Vietnam) and tectonothermal implications: Journal of Asian Earth Sciences, v. 19, no. 1–2, p. 77–84. doi:10.1016/S1367-9120(00)00015-8

Niu, Y., Jiang, B., and Huang, H., 2011, Triassic marine biogeography constrains the palaeogeographic reconstruction of Tibet and adjacent areas: Palaeogeography, Palaeoclimatology, Palaeoecology, v. 306, no. 3–4, p. 160–175. doi:10.1016/j.palaeo.2011.04.016

Patiño Dounce, A.E., 1999, What do experiments tell us about the relative contributions of crust and mantle to the origin of granitic magma? *in* Castro, A., Fernandez, C., and Vigneresse, T.L., eds., Understanding granites: Integrating new and classical techniques: Geological Society of London, Special Publications, p. 55–75.

Patiño Douce, A.E., Humphreys, E.D., and Dana Johnston, A.D., 1990, Anatexis and metamorphism in tectonically thickened continental crust exemplified by the Sevier hinterland, western North America: Earth and Planetary Science Letters, v. 97, p. 290–315. doi:10.1016/0012-821X(90)90048-3

Pearce, J.A., 1983, Role of the sub-continental lithosphere in magma genesis at active continental margins, *in* Hawkesworth, C.J., and Norry, M.J., eds., Continental basalts and mantle xenoliths: Nantwich, Cheshire, Shiva Publication, p. 230–249.

Peng, T.P., Wang, Y.J., Fan, W.M., Liu, D.Y., Shi Y.R., and Miao L.C., 2006, SHRIMP zircon U-Pb geochronology of early Mesozoic felsic igneous rocks from the southern Lancangjiang and its tectonic implications: Science in China Series D: Earth Sciences, v. 49, p. 1032–1042.

Petford, N., Cruden, A.R., McCaffrey, K.J.W., and Vigneresse, J. L., 2000, Granite magma formation, transport and emplacement in the Earth's crust: Nature, v. 408, p. 669–673. doi:10.1038/35047000

Qiu, J.S., McInnes, B.I.A., Xu, X.S., and Allen, C.M., 2004, Zircon ELA-ICP-MS dating for wuliting pluton at Dajishan, southern Jiangxi and new recognition about its relation to tungsten mineralization: Geological Review, v. 50, no. 2, p. 125–133.

Ren, J.S., and Chen, T.Y., 1989, Tectonic evolution of the continental lithosphere in eastern China and adjacent areas: Journal of Southeast Asian Earth Sciences, v. 3, no. 1–4, p. 17–27.

Roger, F., Malavieille, J., Leloup, P.H., Calassou, S., and Xu, Z., 2004, Timing of granite emplacement and cooling in the

Songpan–Garzê Fold Belt (eastern Tibetan Plateau) with tectonic implications: Journal of Asian Earth Sciences, v. 22, no. 5, p. 465–481. doi:10.1016/S1367-9120(03)00089-0

Shabani, A.A.T., Lalonde, A.E., and Whalen, J.B., 2003, Composition of biotite from granitic rocks of the Canadian Appalachian Orogen: A potential tectonomagmatic indicator?: The Canadian Mineralogist, v. 41, p. 1381–1396. doi:10.2113/gscanmin.41.6.1381

Shao, J.G., Peng, S.M., and Peng, S.B., 1995, 40Ar/36Ar-39Ar/36Ar isochron dating for peripheral faults pf Yunkai Massif: Guangdong Geology, v. 10, no. 2, p. 34–40.

Shu, L.S., Faure, M., Wang, B., Zhou, X.M., and Song, B., 2008, Late Palaeozoic-Early Mesozoic geological features of South China: Response to the Indosinian collision events in Southeast Asia: Comptes Rendus Geoscience, v. 340, no. 2–3, p. 151–165. doi:10.1016/j.crte.2007.10.010

Shu, L.S., Zhou, X.M., Deng, P., Wang, B., Jiang, S.Y., Yu, J.H., and Zhao, X.X., 2009, Mesozoic tectonic evolution of the Southeast China Block: New insights from basin analysis: Journal of Asian Earth Sciences, v. 34, p. 376–391. doi:10.1016/j.jseaes.2008.06.004

Sun, L.Q., Ling, H.F., Shen, W.Z., Huang, G.L., and Tan, Z.Z., 2010, Geochronology of Youshan and Pingtian granites in Nanling range and Geological implication: Geological Journal of China Universities, v. 16, no. 2, p. 186–197.

Sun, S.S., and McDonough, W.F., 1989, Chemical and isotopic systematics of oceanic basalt: Implication for mantle composition and processes, *in* Saunders, A.D., and Norry, M.J., eds., Magmatism in the Ocean Basins: The Geological Society of London, Special Publications, v. 42, p. 528–548.

Sun, T., Zhou, X.M., Chen, P.R., Li, H.M., Zhou, H.Y., Wang, Z. C., and Shen, W.Z., 2005, Strongly peraluminous granites of mesozoic in Eastern Nanling Range, Southern China: Petrogenesis and implications for tectonics: Science in China Series D-Earth Sciences, v. 48, no. 2, p. 165–174. doi:10.1360/03YD0042

Sun, W., Li, S., Chen, Y., and Li, Y., 2002, Timing of Synorogenic Granitoids in the South Qinling, Central China: Constraints on the evolution of the Qinling-Dabie Orogenic belt: The Journal of Geology, v. 110, no. 4, p. 457–468. doi:10.1086/340632

Sun, W.D., Ding, X., Hu, Y.H., and Li, X.H., 2007, The golden transformation of the Cretaceous plate subduction in the west Pacific: Earth and Planetary Science Letters, v. 262, no. 3–4, p. 533–542. doi:10.1016/j.epsl.2007.08.021

Sun, W.D., Yang, X.Y., Fan, W.M., and Wu, F.Y., 2012, Mesozoic large scale magmatism and mineralization in South China: Preface: Lithos, v. 150, p. 1–5. doi:10.1016/j.lithos.2012.06.028

Sylvester, P.J., 1998, Post-collisional strongly peraluminous granites: Lithos, v. 45, p. 29–44. doi:10.1016/S0024-4937(98)00024-3

Visonà, D., and Lombardo, B., 2002, Two-mica and tourmaline leucogranites from the Everest-Makalu region (Nepal-Tibet). Himalayan leucogranite genesis by isobaric heating?: Lithos, v. 62, no. 3–4, p. 125–150. doi:10.1016/S0024-4937(02)00112-3

Wang, F.Y., Ling, M., Ding, X., Hu, Y., Zhou, J., Yang, X., Liang, H., Fan, W., and Sun, W., 2011, Mesozoic large magmatic events and mineralization in SE China: Oblique subduction of the Pacific plate: International Geology Review, v. 53, no. 5–6, p. 704–726. doi:10.1080/00206814.2010.503736

Wang, Q., Li, J., Jian, P., Zhao, Z., Xiong, X., Bao, Z., Xu, J., Li, C., and Ma, J., 2005a, Alkaline syenites in eastern Cathaysia (South China): Link to Permian-Triassic transtension: Earth and Planetary Science Letters, v. 230, no. 3–4, p. 339–354. doi:10.1016/j.epsl.2004.11.023

Wang, X., Yao, X.J., and Wang, C.S., 2006, Characteristic mineralogy of the Zhutishi granite: Implication for petrogenesis of the late intrusive granite: Science in China Series D, v. 49, no. 6, p. 573–583. doi:10.1007/s11430-006-0573-4

Wang, Y., Fan, W., Sun, M., Liang, X., Zhang, Y., and Peng, T., 2007, Geochronological, geochemical and geothermal constraints on petrogenesis of the Indosinian peraluminous granites in the South China Block: A case study in the Hunan Province: Lithos, v. 96, no. 3–4, p. 475–502. doi:10.1016/j.lithos.2006.11.010

Wang, Y., Wu, C., Zhang, A., Fan, W., Zhang, Y., Zhang, Y., Peng, T., and Yin, C., 2012, Kwangsian and Indosinian reworking of the eastern South China Block: Constraints on zircon U-Pb geochronology and metamorphism of amphibolites and granulites: Lithos, v. 150, p. 227–242. doi:10.1016/j.lithos.2012.04.022

Wang, Y.J., Fan, W.M., and Guo, F., 2003a, Geochemistry of early Mesozoic potassium-rich diorites-granodiorites in southeastern Hunan Province, South China: Petrogenesis and tectonic implications: Geochemical Journal, v. 37, p. 427–448. doi:10.2343/geochemj.37.427

Wang, Y.J., Fan, W.M., Guo, F., and Li, X., 2001, Petrological and geochemical characteristics of Mesozoic granodioritic intrusions in Southeast Hunan Province, China: Acta Petrologica Sinica, v. 17, no. 1, p. 169–175.

Wang, Y.J., Fan, W.M., Guo, F., Peng, T.P., and Li, C.W., 2003b, Geochemistry of Mesozoic Mafic rocks adjacent to the Chenzhou-Linwu fault, South China: Implications for the lithospheric boundary between the Yangtze and Cathaysia blocks: International Geology Review, v. 45, no. 3, p. 263–286. doi:10.2747/0020-6814.45.3.263

Wang, Y.J., Zhang, Y.H., Fan, W.M., and Peng, T.P., 2005b, Structural signatures and $^{40}Ar/^{39}Ar$ geochronology of the Indosinian Xuefengshan tectonic belt, South China Block: Journal of Structural Geology, v. 27, no. 6, p. 985–998. doi:10.1016/j.jsg.2005.04.004

Watson, E.B., and Harrison, T.M., 1983, Zircon saturation revisited: Temperature and composition effects in a variety of crustal magma types: Earth and Planetary Science Letters, v. 64, p. 295–304. doi:10.1016/0012-821X(83)90211-X

Wones, D.R., and Eugster, H.P., 1965, Stability of biotite: Experiment, theory, and application: American Mineralogist, v. 50, p. 1228–1272.

Wong, W.H., 1929, The Mesozoic orogenic movement in eastern China: Bulletin of the Geological Society of China, v. 8, p. 33–44.

Wu, F.Y., Jahn, B.M., Wilde, S.A., Lo, C.H., Yui, T.F., Lin, Q., Ge, W.C., and Sun, D.Y., 2003, Highly fractionated I-type granites in NE China (I): Geochronology and petrogenesis: Lithos, v. 66, p. 241–273. doi:10.1016/S0024-4937(02)00222-0

Xu, X.S., Deng, P., O'Reilly, S.Y., Griffin, W.L., Zhou, X.M., and Tan, Z.Z., 2003, Single zircon LAM-ICPMS U-Pb dating of Guidong complex (SE China) and its petrogenetic significance: Chinese Science Bulletin: Lithos, v. 48, no. 17, p. 1892–1899.

Yan, D.P., Zhou, M.F., Song, H.L., Wang, X.W., and Malpas, J., 2003, Origin and tectonic significance of a Mesozoic multilayer over-thrust system within the Yangtze Block (South China): Tectonophysics, v. 361, p. 239–254. doi:10.1016/S0040-1951(02)00646-7

Yuan, H.L., Wu, F.Y., Gao, S., Liu, X.M., Xu, P., and Sun, D.Y., 2003, Determination of U-Pb age and rare earth element

concentrations of zircons from Cenozoic intrusions in northeastern China by laser ablation ICP-MS: Chinese Science Bulletin, v. 48, no. 22, p. 2411–2421.

Zhang, F., Wang, Y., Chen, X., Fan, W., Zhang, Y., Zhang, G., and Zhang, A., 2011, Triassic high-strain shear zones in Hainan Island (South China) and their implications on the amalgamation of the Indochina and South China Blocks: Kinematic and 40Ar/39Ar geochronological constraints: Gondwana Research, v. 19, no. 4, p. 910–925. doi:10.1016/j.gr.2010.11.002

Zhang, K.J., 1997, North and South China collision along the eastern and southern North China margins: Tectonophysics, v. 270, no. 1–2, p. 145–156. doi:10.1016/S0040-1951(96)00208-9

Zhang, W.L., Hua, R.M., Wang, R.C., Li, H.M., and Chen, P.R., 2004, Single Ziron U-Pb isotopic age of the Wuliting Granite in Dajishan area of Jiangxi, and its geological implication: Acta Geologica Sinica, v. 78, no. 3, p. 352–258.

Zhao, Z.H., Bao, Z.W., and Zhang, B.Y., 1998, Geochemistry of the Mesozoic basaltic rocks in southern Hunan Province: Science in China Series D: Earth Sciences, v. 41, p. 102–112. doi:10.1007/BF02875640

Zhou, X.M., and Li, W.X., 2000, Origin of Late Mesozoic igneous rocks in Southeastern China: Implications for lithosphere subduction and underplating of mafic magmas: Tectonophysics, v. 326, no. 3–4, p. 269–287. doi:10.1016/S0040-1951(00)00120-7

Zhou, X.M., Sun, T., Shen, W.Z., Shu, L.S., and Niu, Y.L., 2006, Petrogenesis of Mesozoic granitoids and volcanic rocks in South China: A response to tectonic evolution: Episodes, v. 29, no. 1, p. 26–33.